LA-10848-T
Thesis

UC-34
Issued: October 198

LA--10848-T

DE87 002246

Analyzing Powers and Proton Spin Transfer Coefficients in the Elastic Scattering of 800 MeV Polarized Protons from an L-Type Polarized Deuteron Target at Small Momentum Transfers

David Laurence Adams

DISCLAIMER

This report was prepared as an account of work sponsored by an agency of the United States Government. Neither the United States Government nor any agency thereof, nor any of their employees, makes any warranty, express or implied, or assumes any legal liability or responsibility for the accuracy, completeness, or usefulness of any information, apparatus, product, or process disclosed, or represents that its use would not infringe privately owned rights. Reference herein to any specific commercial product, process, or service by trade name, trademark, manufacturer, or otherwise does not necessarily constitute or imply its endorsement, recommendation, or favoring by the United States Government or any agency thereof. The views and opinions of authors expressed herein do not necessarily state or reflect those of the United States Government or any agency thereof.

MASTER

Los Alamos National Laboratory
Los Alamos, New Mexico 87545

DISTRIBUTION OF THIS DOCUMENT IS UNLIMITED

TABLE OF CONTENTS

ANALYZING POWERS AND PROTON SPIN TRANSFER COEFFICIENTS
IN THE ELASTIC SCATTERING OF 800 MeV POLARIZED PROTONS
FROM AN L-TYPE POLARIZED DEUTERON TARGET AT SMALL MOMENTUM TRANSFERS

by

David Laurence Adams

ABSTRACT

Analyzing powers and spin transfer coefficients which describe the elastic scattering of polarized protons from a polarized deuteron target have been measured. The energy of the proton beam was 800 MeV and data were taken at laboratory scattering angles of 7, 11, 14, and 16.5 degrees. One analyzing power was also measured at 180 degrees. Three linearly independent orientations of the beam polarization were used and the target was polarized parallel and antiparallel to the direction of the beam momentum. The data were taken with the high resolution spectrometer at the Los Alamos Meson Physics Facility (experiment 685). The results are compared with multiple scattering predictions based on Dirac representations of the nucleon-nucleon scattering matrices.

I. Introduction

Proton-deuteron elastic scattering at medium energies (~ 1 GeV) is sensitive to both the structure of the deuteron and the medium energy nucleon-nucleon scattering matrices. The latter are interesting because they provide information about the internal structure of the nucleons and because they are an essential ingredient in the description of medium energy nucleon-nucleus scattering. Because the deuteron consists of only two nucleons, it should be possible to obtain a theoretical understanding of its structure which is more complete than that for any other nucleus. Of course, there are many other experiments which are sensitive to either the deuteron structure or the nucleon-nucleon matrices and it is not necessary to extract both from these measurements alone. Proton-deuteron elastic scattering also tests the different reaction mechanisms used to describe both this and other proton-nucleus scattering processes.

Other readily available probes for studying the deuteron structure include the electron and the pion. The electron provides a relatively clean probe because it appears to have no internal structure but it is sensitive only to the electromagnetic structure of the deuteron. Thus, experiments performed with electrons are complementary to those making use of strongly interacting particles like the proton and pion. Pions are not available with the same intensity or range of energies as the proton. Also, because the pion has no spin, it is necessary to polarize the deuteron target or

measure the spin of the recoil deuteron to determine anything beyond the unpolarized cross section for the elastic reaction.

The on-shell nucleon-nucleon scattering matrices can be determined directly in proton-proton and proton-neutron scattering experiments. However, the proton-neutron matrix is not completely determined in our energy range because of the difficulties inherent in doing experiments with a neutral particle. Perhaps most interesting is that proton-deuteron elastic scattering and other medium energy proton-nucleus interactions are sensitive to the additional off-shell pieces of the nucleon-nucleon scattering matrices which appear when they are expressed in terms of the relativistic Dirac operators instead of the usual Pauli operators. Early applications of such nucleon-nucleon matrices to the scattering of of protons from spin zero nuclei are given in references 1-4. The predictions based on the relativistic matrices are different and often in better agreement with experiment than those made with the traditional nonrelativistic forms. There also can be significant differences between relativistic and nonrelativistic predictions for spin observables in proton-deuteron elastic scattering.[5] Different relativistic models also produce different predictions.[6]

The spin structure of the proton-deuteron elastic reaction is quite complicated. Assuming invariance under parity and time reversal, the scattering matrix includes 12 independent complex functions of energy and momentum transfer. Thus, to completely determine the matrix up to an overall phase, it is necessary to

measure at least 23 independent observables. However, there are only six linearly independent observables which can be determined in experiments where the incident deuteron is not polarized and the polarization of the scattered deuteron is not measured. These include the unpolarized cross section, either the analyzing power or induced proton polarization, and four Wolfenstein parameters.[7] The latter are essentially the elements of the rotation matrix which connect the incoming and outgoing proton polarizations. There is much additional information contained in observables which involve the polarization of the deuteron.

For this reason, we are performing a series of experiments with polarized deuteron targets. Here we describe a small angle experiment ($5 < \theta_{lab} < 20°$) performed with a deuteron target polarized parallel to the momentum of the incident polarized proton beam. Assuming parity invariance, we have measured the two analyzing powers and six proton spin transfer coefficients which involve the vector polarization of the target. We have also made a rough measurement of the analyzing power which connects the tensor polarization of the target with the beam polarization. In addition to these small momentum transfer observables, we have determined for backward scattering the one analyzing power which involves the vector polarization of the target.

II. Formalism

In order to make the connection between our experimental data and theoretical calculations, we define a set of observables, the C-coefficients. We first introduce a coordinate system and two sets of spin operators to describe the spin 1/2 proton and spin 1 deuteron.

Coordinate Systems

We define two spatial coordinate systems – one to describe the spins of the incident particles and a second for the scattered proton. In both cases we define a right handed orthonormal basis ($\hat{S}$, $\hat{N}$, $\hat{L}$). The longitudinal vector $\hat{L}$ is parallel to the momentum of the incident proton, $\underset{\sim}{k}_i$, in the first system and parallel to the scattered proton momentum, $\underset{\sim}{k}_f$, in the second. The normal direction $\hat{N}$ is the same in both systems and points perpendicular to the scattering plane along the direction $\underset{\sim}{k}_i \times \underset{\sim}{k}_f$. The sideways direction is defined by $\hat{S} = \hat{N} \times \hat{L}$. Because the momenta change sign under a parity transformation, $\hat{S}$ and $\hat{L}$ also change sign and $\hat{N}$ is unaffected.

Spin 1/2

Denote a complete set of four spin 1/2 operators by σ_a where a = 0,S,N,L. Here σ_0 is the unit operator and $\sigma_i = \underset{\sim}{\sigma} \cdot \hat{i}$ (i = S,N,L) where $\underset{\sim}{\sigma}$ is the usual Pauli operator. Because this operator describes

angular momentum, it does not change sign under a parity transformation and σ_S and σ_L change sign under parity while σ_0 and σ_N do not.

If a system of spin 1/2 particles (e.g., the incident beam or scattered protons) is described by the density matrix $\hat{\rho}$, then the polarization of the system is described by the vector $\underset{\sim}{p} = (p_S, p_N, p_L)$ where $p_i = \langle\sigma_i\rangle = \mathrm{tr}(\hat{\rho}\sigma_i)/\mathrm{tr}(\hat{\rho})$. The density matrix can be expressed in terms of the spin operators and the components of polarization:

$$\hat{\rho} = \frac{1}{2}\,(1 + p_S\sigma_S + p_N\sigma_N + p_L\sigma_L)\ .$$

Spin 1

We denote an overcomplete set of ten spin one operators by J_α where $\alpha = 0,S,N,L,SN,SL,NL,SS,NN,LL$. Here J_0 is the unit operator, $J_i = \underset{\sim}{J}\cdot\hat{i}$ $(i = S,N,L)$ are the components of the usual spin one angular momentum operator $\underset{\sim}{J}$, and the symmetric tensor operators are defined by $J_{ij} = \frac{3}{2}(J_iJ_j + J_jJ_i) - 2\delta_{ij}$. This set of operators is overcomplete because $J_{SS} + J_{NN} + J_{LL} = 0$. Because the angular momentum operator is invariant under parity, those operators in which either but not both of the indices S and L appear an odd number of times (J_S, J_{NL}, ...) change sign under a parity transformation while those remaining (J_0, J_N, J_{SL}, ...) do not.

An arbitrary mixture of spin one particles can be described by the density matrix $\hat{\rho}$ with components of polarization given by $p_\alpha = \langle J_\alpha \rangle = tr(\hat{\rho}J_\alpha)/tr(\hat{\rho})$. Although there are ten equations here, the first is trivial, $p_0 = 1$, and the relationship $p_{SS} + p_{NN} + p_{LL} = 0$ follows from the similar equation for the spin operators. Thus, there are eight independent polarizations (three vector and five tensor) which describe a system of spin one particles. However, for the case of a system with a symmetry axis, there are only two independent polarizations (one vector and one tensor). In our case, where the deuteron target polarization is cylindrically symmetric about the $\hat{L}$ direction, the density matrix can be written as

$$\hat{\rho} = \frac{1}{3}\left(1 + \frac{3}{2}PJ_L + \frac{1}{2}P_T J_{LL}\right)$$

where $P = p_L$ is the vector polarization and $P_T = p_{LL}$ is the tensor polarization.

Observables

The definitions for the observables follow naturally from the introduction of the scattering matrix which contains all information about the scattering process. The construction of this operator is generally the aim of a theoretical calculation. The scattering matrix $\hat{F}$ operates in the spin space of both particles connecting the incoming state $|i\rangle$ to the scattered state $|o\rangle = \hat{F}|i\rangle$. The density matrix

describing the outgoing state is connected to that of the incoming state by $\hat{\rho}_{out} = \hat{F}\,\hat{\rho}_{in}\,\hat{F}^{+}$.

Because the beam and target are prepared independently, the density matrix describing the initial combined spin state is the product of the incoming proton and deuteron density matrices:

$$\hat{\rho}_{in} = \frac{1}{6}\,(1 + p_S\sigma_S + p_N\sigma_N + p_L\sigma_L)\,(1 + \frac{3}{2}pJ_L + \frac{1}{2}p_T J_{LL})$$

The yield or cross section is given by $Y = tr(\hat{\rho}_{out})$ and the outgoing proton polarizations are given by $p_i' = tr(\hat{\rho}_{out}\sigma_i)/tr(\hat{\rho}_{out})$ $(i = S,N,L)$.

The observables, the C-coefficients, are defined by

$$C_{a\alpha,b\beta} = \frac{tr(\hat{F}\sigma_a J_\alpha \hat{F}^{+}\sigma_b J_\beta)}{tr(\hat{F}\hat{F}^{+})}$$

and we make use of the abbreviated notation $A_{a\alpha} = C_{a\alpha,00}$ and $C_{a\alpha,b} = C_{a\alpha,b0}$ to reduce the number of indices. Those coefficients in which either but not both of the indices S and L appear an odd number of times (A_{S0}, $C_{SLL,N}$, $C_{0L,SS}$, ...) change sign under parity and must vanish because we assume invariance under the transformation. The yield and outgoing polarizations can be expressed in terms of the observables and the incoming polarizations. For an L-type deuteron target and a proton beam with arbitrary polarization, the yield is given by

$$Y = Y_0[1 + A_{NO}P_N + \frac{3}{2}A_{SL}P_S P + \frac{3}{2}A_{LL}P_L P + \frac{1}{2}A_{OLL}P_T + \frac{1}{2}A_{NLL}P_N P_T] \quad (1)$$

and the components of the scattered proton's polarization are

$$P'_S = \frac{Y_0}{Y}\left[\frac{3}{2}C_{OL,S}P + (C_{SO,S} + \frac{1}{2}C_{SLL,S}P_T)P_S + \frac{3}{2}C_{NL,S}PP_N + (C_{LO,S} + \frac{1}{2}C_{LLL,S}P_T)P_L\right]$$

$$P'_N = \frac{Y_0}{Y}\left[(C_{OO,N} + \frac{1}{2}C_{OLL,N}P_T) + \frac{3}{2}C_{SL,N}PP_S + (C_{NO,N} + \frac{1}{2}C_{NLL,N}P_T)P_N + \frac{3}{2}C_{LL,N}PP_L\right]$$

$$P'_L = \frac{Y_0}{Y}\left[\frac{3}{2}C_{OL,L}P + (C_{SO,L} + \frac{1}{2}C_{SLL,L}P_T)P_S + \frac{3}{2}C_{NL,L}PP_N + (C_{LO,L} + \frac{1}{2}C_{LLL,L}P_T)P_L\right]. \quad (2)$$

Here Y_0 is the yield for unpolarized beam and target.

Analyzing Powers

We collectively refer to the coefficients $A_{a\alpha}$ as analyzing powers. We are sensitive to five of these in this experiment but, because the tensor polarization of the target is quite small, the sensitivity to either A_{OLL} or A_{NLL} is weak. The usual uncorrelated proton analyzing power A_{NO} has been measured previously[8-10] and we present our results as a check. The analyzing powers of interest are A_{SL} and A_{LL}.

The extraction of the analyzing powers directly from equation 1 requires the measurement of the relative cross section for a variety of beam and target polarizations. This would require relative normalization of the beam intensity and effective target thickness over the course of the entire experiment. We obtain much greater precision by measuring only the asymmetry due to the beam polarization,

$$\varepsilon = \frac{Y(\underset{\sim}{p}) - Y(-\underset{\sim}{p})}{Y(\underset{\sim}{p}) + Y(-\underset{\sim}{p})}$$

$$= \frac{A_{NO}P_N + \frac{3}{2}A_{SL}P_S P + \frac{3}{2}A_{LL}P_L P + \frac{1}{2}A_{NLL}P_N P_T}{1 + \frac{1}{2}A_{OLL}P_T} . \qquad (3)$$

This asymmetry does not depend on any long term normalization because the direction of the beam polarization was reversed every couple minutes.

The analyzing power A_{OLL} has been previously measured.[11] Equation 3 can be used to evaluate some or all of the remaining analyzing powers provided we have a sufficient number of independent measurements. Each measurement must include the beam and target polarization as well as the asymmetry.

Spin Transfer Coefficients

We refer to the parameters $C_{a\alpha,b}$ $(b \neq 0)$ as spin transfer coefficients. These require measurement of the polarization of the scattered proton as well as that of the beam and target. The evaluation of these coefficients is complicated because we cannot distinguish proton-deuteron elastic and background events when we measure the polarization of the scattered protons. However, because the background events involve scattering from unpolarized materials (primarily carbon and oxygen), the cross section and the polarization of the scattered proton have a relatively simple dependence on the incoming polarization:

$$Y = Y_0[1 + D_{NO}p_N]$$

$$p'_S = \frac{Y_0}{Y}[D_{SS}p_S + D_{LS}p_L]$$

$$p'_N = \frac{Y_0}{Y}[D_{ON} + D_{NN}p_N]$$

$$p'_L = \frac{Y_0}{Y}[D_{SL}p_S + D_{LL}p_L] \ .$$

These relations are analogous to equations 1 and 2 with D_{NO}, D_{ON}, and D_{ij} replacing A_{NO}, $C_{OO,N}$, and $C_{iO,j}$. These coefficients do not describe a single reaction but are an average over all the reactions which make up the unpolarized background. A more precise definition of these coefficients and the justification for treating them as constant are given in appendix A.

Denote the proton-deuteron elastic and background yields by Y(d) and Y(bg) and their sum by Y(tot). The measured polarization will be a combination of that due to proton-deuteron elastic events and that from the background

$$p' = \frac{Y(d)}{Y(tot)}\, p'(d) + \frac{Y(bg)}{Y(tot)}\, p'(bg) \ .$$

Assuming invariance under parity, the outgoing polarization may be written (i,j = S,N,L)

$$p'_j = M_{0j} + \Sigma\, M_{ij}\, p_i \qquad (4)$$

$$\begin{aligned}
M_{OS} &= \frac{3}{2} R\, C_{OL,S}\, P \\
M_{ON} &= R\, [C_{OO,N} + \frac{1}{2} C_{NLL,N}\, P_T + r\, D_{ON}] \\
M_{OL} &= \frac{3}{2} R\, C_{OL,L}\, P \\
M_{SS} &= R\, [C_{SO,S} + \frac{1}{2} C_{SLL,S}\, P_T + r\, D_{SS}] \\
M_{NS} &= \frac{3}{2} R\, C_{NL,S}\, P \\
M_{LS} &= R\, [C_{LO,S} + \frac{1}{2} C_{LLL,S}\, P_T + r\, D_{LS}] \\
M_{SN} &= \frac{3}{2} R\, C_{SL,N}\, P \\
M_{NN} &= R\, [C_{NO,N} + \frac{1}{2} C_{NLL,N}\, P_T + r\, D_{NN}] \\
M_{LN} &= \frac{3}{2} R\, C_{LL,N}\, P \\
M_{SL} &= R\, [C_{SO,L} + \frac{1}{2} C_{SLL,L}\, P_T + r\, D_{SL}] \\
M_{NL} &= \frac{3}{2} R\, C_{NL,L}\, P \\
M_{LL} &= R\, [C_{LO,L} + \frac{1}{2} C_{LLL,L}\, P_T + r\, D_{LL}] \ .
\end{aligned}$$

Here $R = Y_0(d)/Y(tot)$ and $r = Y_0(bg)/Y_0(d)$. The subscript 0 indicates the yield is that for unpolarized beam and target.

At the focal plane, we are able to measure only two of the three components of the polarization of the scattered proton but these are both mixtures of all three of the components at the target. We are sensitive to all 12 of the elements M_{ia} (i = S,N,L, a = 0,S,N,L) which appear in equation 4. Six of the elements contain only one observable and depend on the vector polarization of the target. These observables are the six spin transfer coefficients of interest: $C_{OL,S}$, $C_{OL,L}$, $C_{NL,S}$, $C_{SL,N}$, $C_{LL,N}$, and $C_{NL,L}$.

In each of the remaining terms, a proton-deuteron elastic observable which does not depend on the target polarization appears in combination with one which depends on the tensor polarization and with a background coefficient. Again, because the tensor polarization was quite small and always had the same sign, there is little sensitivity to the six tensor observables ($C_{NLL,N}$, $C_{SLL,S}$, ...). The ratio r does not depend on the beam polarization and did not vary significantly between runs. Consequently, we are not able to separate the remaining proton-deuteron elastic observables (the induced polarization $C_{OO,N}$ and the five Wolfenstein parameters $C_{iO,j}$) from the same observables for the background. We can only determine the linear combinations (M_{ON}, M_{SS}, ...) which are defined in equation 4. These last six observables have been measured previously using data with virtually no background.[10]

Summary

Our data allow us to extract the two analyzing powers and six spin transfer coefficients which involve the L-component of the incoming deuteron vector polarization. The analyzing power involving the LL-component of the tensor polarization is also determined but with much greater uncertainty. Measurement of the beam and target polarization is necessary for all observables. The determination of the analyzing powers also requires the measurement of the asymmetry due to the beam polarization for each orientation of beam and target polarizations. The extraction of the spin transfer coefficients requires the additional measurement of two components of the scattered proton's polarization and the yield ratio R for each orientation.

III. Experimental Conditions

The data discussed here constitute the second part of LAMPF experiment 685 and were taken during August and September of 1984. Polarized 800 MeV protons were scattered from an L-type polarized deuteron target and the yield and outgoing polarization of the scattered protons were measured at the focal plane of the high resolution spectrometer (HRS).

Beam

We made use of the LAMPF polarized proton (p-) beam[12] which is produced by a Lamb shift ion source. The beam is not completely polarized because, at the source, only the hydrogen atoms in the 2S state are fully polarized while the background of ground state ions are almost unpolarized. The contribution from the background varies from 15-30% and has been measured to have a polarization of about 3% in the direction opposite that of the remainder of the beam.[12] It is possible to measure the relative intensity of this background by detuning the source so that no 2S atoms are produced. This is referred to as the quench cycle. The magnitude of the polarization can be calculated by comparing the intensity of the polarized beam, I_p, with that during the quench cycle, I_q:

$$p = 1 - 1.03 \frac{I_q}{I_p} .$$

A polarization of nearly equal magnitude but opposite sign is obtained by reversing the direction of the magnetic field in the source. The two polarized states are referred to as normal and reverse beam. It is easy to change from any of the states (normal, reverse, or quenched) to any other in a few seconds. During our run, the polarization was reversed every two minutes with a quench cycle of approximately five seconds between each reversal.

The polarized protons are accelerated as H- ions. After exiting the source, the ions are accelerated to 0.75 MeV by a Cockroft-Walton accelerator which injects them into an Alvarez drift tube accelerator. There the beam energy is increased to 100 MeV and this beam is injected into the main accelerator where the energy can be increased to a maximum of 800 MeV in a series of side-coupled cavities. The total length of the accelerators is about 800 meters. At 800 MeV, a much more intense unpolarized H+ beam is accelerated along with the polarized beam and these are separated in a switchyard which diverts the polarized beam into line X.

At the end of line X, the polarized H- beam passes through a wire or grid which strips the electrons from some fraction of the beam. The fraction converted to protons is easily varied by changing the stripper. The protons are then separated from the rest of the beam by a pair of bending magnets which deflect them into line C. Three additional bending magnets steer this beam toward the HRS and provide a momentum dispersion of 22 cm/%. The bending magnets are followed by a series of five quadrupole magnets which rotate the beam so that the

dispersion is in the vertical direction. This is necessary because the vertical spectrometer is dispersion matched. These and other quadrupole magnets in lines X and C are used to focus the beam. Small adjustments to the position of the beam are made with steering magnets located at various positions in the beam lines. Between the last two quadrupole magnets and about ten meters before the target, the beam passes through the line C polarimeter. Two ion chambers directly behind the target intercept all of the beam and are used to monitor the intensity. Figure 1 shows the beam transport system from the end of the accelerator to the HRS.

We made use of three different orientations of the beam polarization. The coordinate system used to specify the polarization at the polarimeter is such that $\hat{L}$ points along the direction of the beam momentum, $\hat{N}$ points upward, and $\hat{S} = \hat{N} \times \hat{L}$; i.e., to the left facing downstream. This polarization was in the SL plane about 60 degrees from $\hat{L}$ for the first two weeks. The two orientations for the next five and last seven days were both in the NL plane about 50 degrees from $\hat{L}$. See figure 2.

We ran with a beam intensity of about 5×10^6 protons/sec at seven degrees and 2×10^7 at the other angles. The intensity at the larger angles was limited to minimize the depolarization of the target. The intensity at seven degrees allowed us to write 200-300 events/sec to tape and the lowest data acquisition rate was about 50 events/sec at 16.5 degrees.

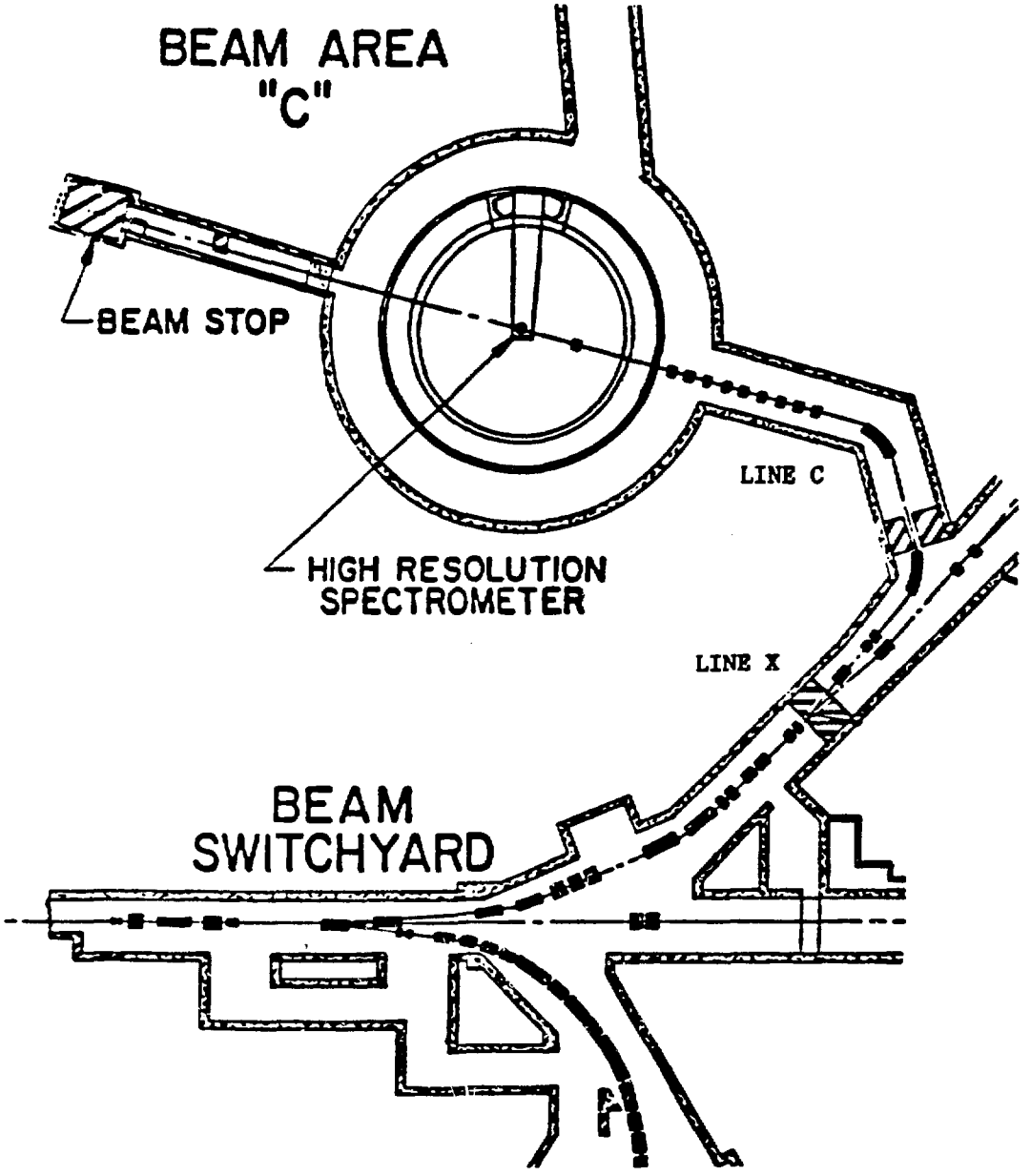

Figure III-1

Switchyard, line X, and line C.

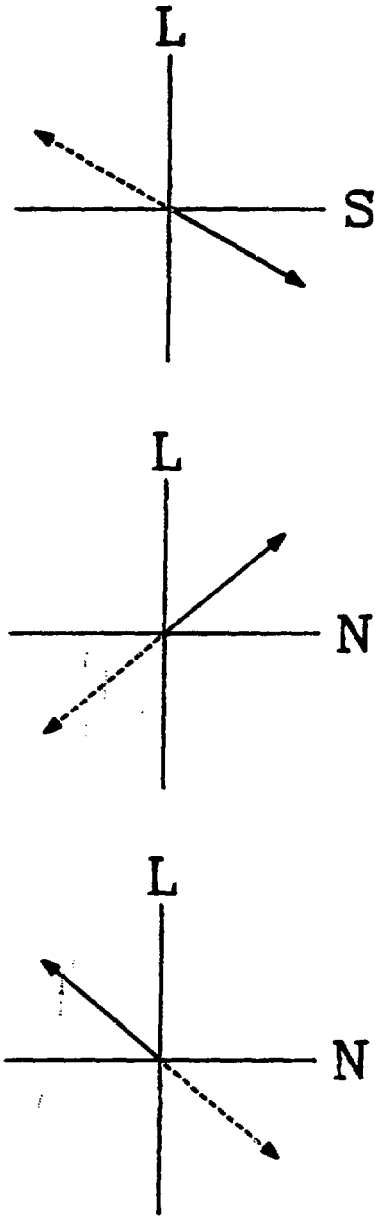

Figure III-2

The three orientations of the beam polarization at the line C polarimeter. The solid line is the normal beam state and the dashed line is the reverse. In each case, the missing component was very close to zero.

The beam at the HRS target is 2-3 mm wide and can have a height up to about 2 cm. In order to minimize the intensity on any one region of the target, a steering magnet was used to sweep the beam back and forth in the horizontal direction. The range of motion was about 4 mm to either side. The height of the beam was about 2 cm to match that of the target. The position and size of the beam were checked regularly between runs by inserting a small wire chamber into the beam near the target. This beam spot and the maximum intensity quoted above correspond to a flux of about 1×10^7 protons/sec/cm^2.

The ion chambers behind the target used to monitor the beam intensity are filled with a mixture of helium (90%) and carbon dioxide (10%) for most HRS experiments. However, because of the low beam intensities during our runs, we ran with only krypton in one chamber and only xenon in the other. The accumulated charge was summed with special integrators which have a sensitivity of 10^{-11} coulombs. These conditions enabled us to obtain an output pulse from either integrator with about 5×10^5 protons.

Target

We used the KEK polarized target in a spin frozen mode. The target material was fully deuterated propanediol in the form of small beads in a ^{3}He/^{4}He liquid bath. This bath provided a dilution refrigerator which kept the target temperature at about 50 mK. The target was centered in the superconducting R and A magnet which was

operated with a central field of 10 kgauss. The beam travelled along the axis of the magnet such that the field was in the same direction as the beam momentum.

The target was repolarized every one to four days and an NMR measurement of the polarization was made before and after each polarization. A few measurements were also made without repolarizing. For polarization and measurement of the polarization, the central field of the magnet was increased to 25 kgauss. The target could be polarized either parallel or antiparallel to the beam momentum and approximately equal amounts of data were taken with the two directions at each angle for each orientation of the beam polarization. Figure 3 shows the target flask, the walls of the target cryostat, and the beam. The target was fairly thick (> 2 cm) to obtain a sufficiently large yield with the low beam intensities required to keep the target from depolarizing. The cryostat walls were replaced with thin windows over much of the area where they intercepted either the incoming beam or the the trajectories of particles scattered into the acceptance of the spectrometer.

Reasonable care was taken to ensure that the region in which the beam intercepted the target was within the limited acceptance of the spectrometer. X-rays were taken to determine the position of the target inside the cryostat and the cryostat was surveyed into place. Before taking any other data, we did some scattering measurements to check the positions of the target and beam. A steering magnet was used to place the beam at different horizontal positions on the target

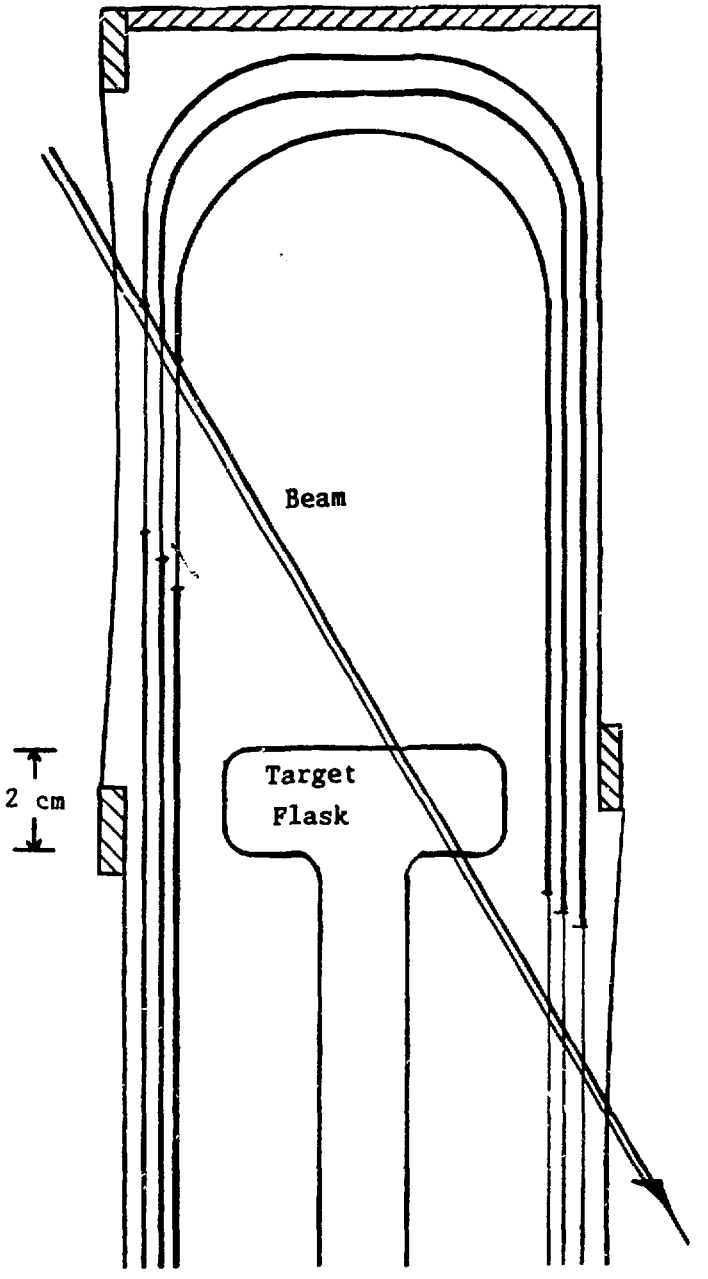

Figure III-3

Horizontal cross section of the target flask, the cryostat walls and windows, and the beam.

and the yield was measured both with the spectrometer set at 20 degrees and with scintillator telescopes located above and below the target. The target was moved 5 mm downstream as a result of these measurements and the yields were measured again. The results of the these final measurements are presented in figure 4. From this figure, we see that the HRS yield began to decrease about 5 mm on either side of the central beam position. The yield from the scintillator telescopes began to decrease about 5 mm to the left and began to increase 5 mm on the right side. This increase was expected because, on the right side, the beam can pass through additional propanediol contained in the neck of the target. These final results are consistent with the desired positioning of the target.

Detectors

The HRS is a vertical, dispersion matched, QDD spectrometer with a total bend of 150 degrees (see figure 5). The spectrometer can be moved on a circular track over a wide range of horizontal scattering angles. The angular acceptance of the spectrometer is about ±1 degree in horizontal direction and ±2 degrees in the vertical. The focusing is point-to-point in the vertical and parallel-to-point in the horizontal. At 800 MeV, the full energy acceptance is about 35 MeV at the focal plane and an additional scintillator, SX, can be added to the trigger to reduce this acceptance to 20 MeV.

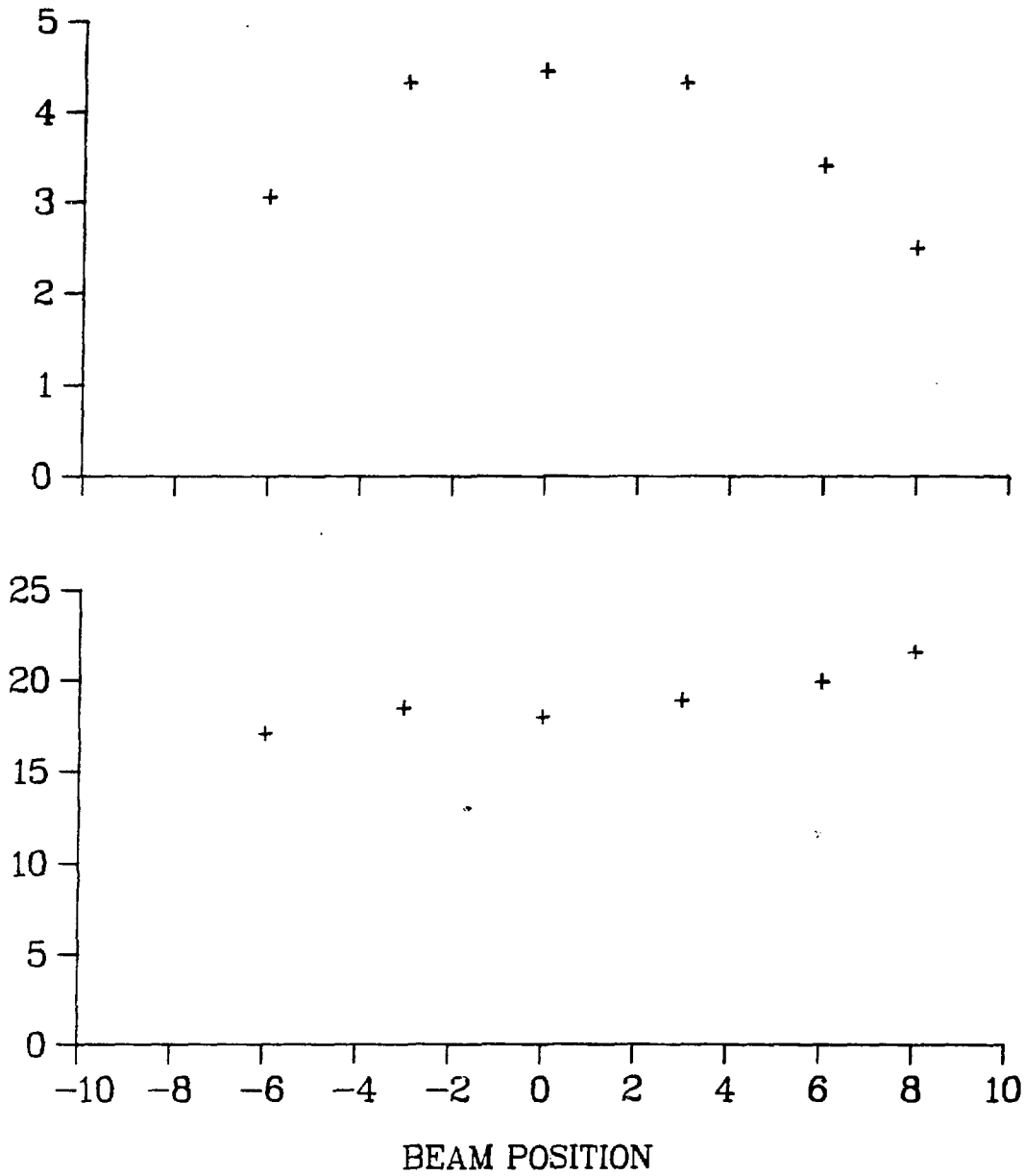

Figure III-4

Yield obtained with the HRS (top) and with the scintillator telescopes (bottom) as a function of beam position. The units on the horizontal axis are mm and are positive when the beam was moved to the right facing downstream.

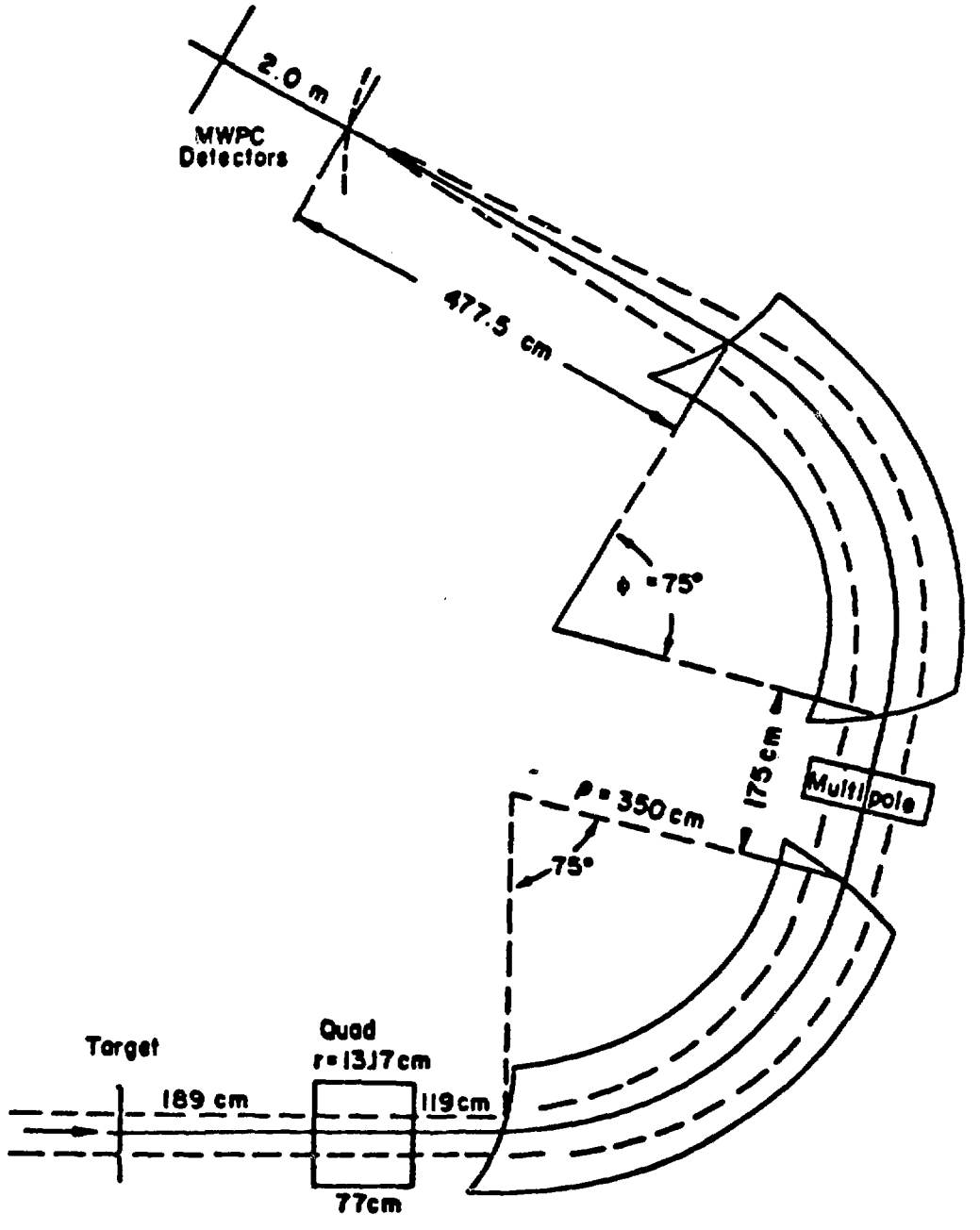

Figure III-5

High resolution spectrometer. We did not make use of the multipole between the two bending magnets.

We took data with the HRS set at 7, 11, 14, and 16.5 degrees. These are the horizontal scattering angles at the center of the angular acceptance. The central vertical scattering angle would have been zero if the magnetic field used to maintain the target polarization had not been present. Because the proton-deuteron elastic cross section falls rapidly with increasing scattering angle in this region (about a factor of two in two degrees), the event averages of the (polar) scattering angles were about 0.2 degrees less than the HRS angles.

The positions of the scintillators, chambers, and carbon blocks at the focal plane are shown in figure 6. The front scintillators S1 and S2 are 10 x 56 cm^2 and the rear scintillators SP1 and SP2 are 38 x 76 cm^2 and overlap by about 3 cm. One trigger used to start the TDC's and ADC's was given by a coincidence between S1, S2, and either SP1 or SP2, i.e., $S1 \cdot S2 \cdot (SP1+SP2)$. The vertical acceptance was reduced for some runs by including SX in the trigger, i.e., by using the trigger $SX \cdot S1 \cdot S2 \cdot (SP1+SP2)$. SX is 10 x 30 cm^2 and was positioned directly behind S1.

There are two delay line drift chambers in front of the carbon blocks and two behind. Each chamber consists of two pairs of planes - one pair with horizontal wires and the other with vertical wires. The two planes in each pair are offset by half a wire spacing to resolve the left-right ambiguity. The front chambers (i.e., those in front of the carbon blocks) are 10 x 60 cm^2 and the rear chambers are 60 x 60 cm^2. The second, third, and fourth chambers are located 50,

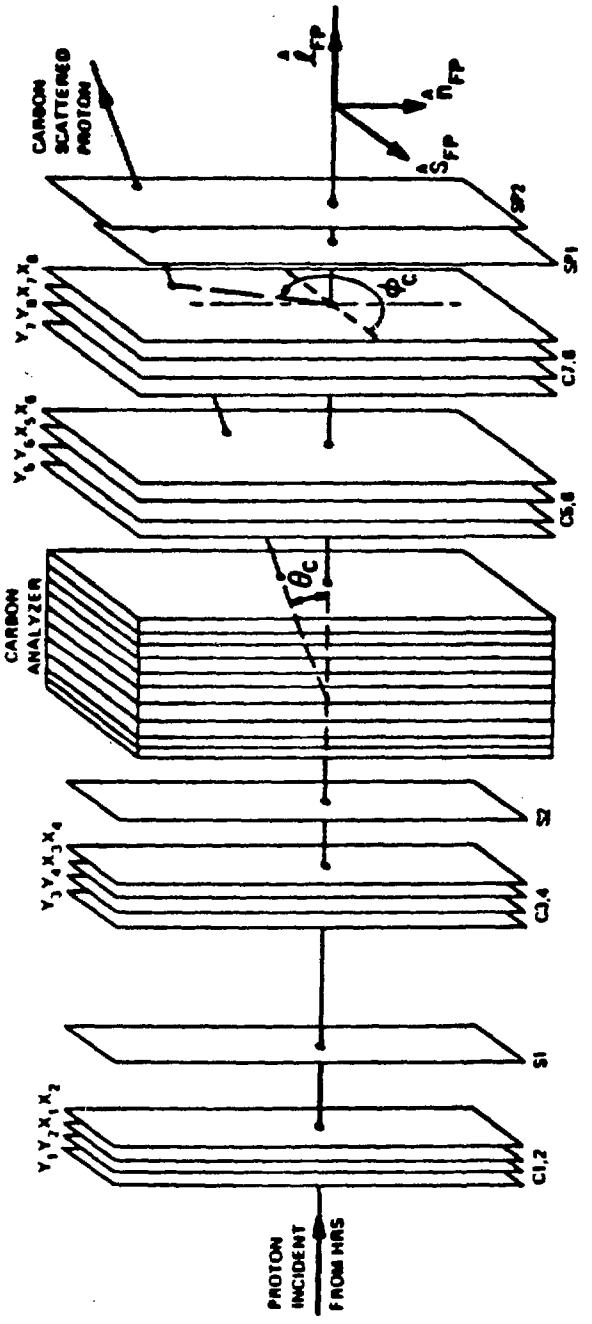

Figure III-6

Arrangement of scintillators, chambers, and carbon blocks at the focal plane. Also shown are the definitions of the carbon scattering angles and the carbon scattering frame.

116, and 141 cm behind the first chamber. The wire spacing in all planes is 0.081 cm.

The carbon blocks are 41 x 65 x 3 cm^3 and can be added or removed singly. We used nine blocks.

The front chambers determine the trajectory of particles coming out of the spectrometer before rescattering in the carbon blocks. This trajectory is used to calculate the momentum transfer, the horizontal and vertical scattering angles, and the y-component of the scattering point at the target. (At the target, y lies in the horizontal plane and is orthogonal to the beam direction.) The polar and azimuthal scattering angles at the target are calculated from the horizontal and vertical angles. The momentum transfer and (polar) scattering angle are used to calculate the missing mass for a particular reaction – in our case d(p,p).

The rear chambers determine the trajectory after rescattering. This trajectory is combined with that from the front chambers to reconstruct the polar and azimuthal scattering angles in the carbon. These angles are used to calculate the two components of polarization perpendicular to the incident direction of motion.

The data used to calculate the focal plane polarizations (FPP data) were taken with a cut utilizing fast rejection circuitry in the microprogrammable branch driver (MBD). Most events which had polar carbon scattering angles of less than approximately 2 degrees were not

written to tape. These events are not useful because the carbon analyzing power is very small at small angles. One event in twenty was flagged and written to tape without being subjected to the MBD test. These events were used for alignment of the rear chambers. The data used to calculate the asymmetries were taken without the MBD cut.

Because the energy of the scattered proton is strongly correlated to the angle for larger scattering angles, the 20 MeV acceptance of the trigger with SX in was not considered adequate in all cases. All seven degree data and the 11 and 14 degree FPP data were taken with SX in the trigger but the remaining data with the exception of two of the 14 degree asymmetry runs were taken without SX.

IV. Beam Polarization

The beam polarization at the line C polarimeter (LCPO) is expressed in terms of the magnitude of the beam polarization, p, the ratio of the N-component to the magnitude, $r_N = p_N/p$, and the S-component ratio, $r_S = p_S/p$. The polarization at the target is obtained by rotating the polarization at the LCPO about the beam axis by the angle θ_p to account for precession in the field of the holding magnet. In addition, because the scattered protons are deflected downward in the holding field, the protons entering at the center of the spectrometer entrance have scattered upward. Therefore, the central scattering plane is rotated about the beam axis by an angle θ_o relative to the horizontal plane.

The beam polarization at the target is expressed in the incoming coordinate system defined in chapter II with the outgoing momentum corresponding to the trajectory which passes through the center of the HRS acceptance. The components of polarization in this frame are

$$p_S = p \left[r_S \cos(\theta_p+\theta_o) + r_N \sin(\theta_p+\theta_o) \right]$$

$$p_N = p \left[-r_S \sin(\theta_p+\theta_o) + r_N \cos(\theta_p+\theta_o) \right]$$

$$p_L = \pm p \left[1 - r_S^2 - r_N^2 \right]^{1/2} .$$

The event average of the beam polarization differs slightly from this central value because of the finite acceptance of the HRS. Appropriate corrections are discussed in appendix B.

Magnitude

The magnitude of the beam polarization was obtained from quench measurements taken simultaneously with the asymmetry and outgoing polarization data. The quench measurement of the beam polarization is discussed in chapter III. The beam intensity was monitored by the two ion chambers behind the target and by counting triggers in the HRS. Both were normalized by dividing by the number of beam cycles. Because the number of triggers is sensitive to the beam polarization, normal and reverse beam intensities were calculated separately and then averaged to obtain the polarized intensity.

The statistical uncertainties in these measurements are quite small but the quench measurements are subject to other errors which are difficult to evaluate precisely. Most important is the normalization which can be off if there are many empty cycles or if the beam intensity is changing on a time scale of a few minutes. We have assigned an uncertainty of 0.02 to the the quench measurement for each series of runs taken at a given HRS angle with particular orientations of the beam and target polarizations.

Direction

The ratios r_N and r_S were measured during special runs taken regularly throughout the data acquisition. A CH_2 target was inserted into the line C polarimeter for these runs allowing measurement of the

S- and N-components of the beam polarization along with the quench measurement of the magnitude. The ratios were obtained by dividing the polarimeter measurements by the quench result.

The general features of the line C polarimeter are the same as those of the other beam line polarimeters at LAMPF which are described in reference 13. The N-component of the beam polarization is determined by four arms in the horizontal plane containing the beam. Each arm is a telescope consisting of two small scintillator counters. On both the left and right sides of the beam, there is a forward arm centered at 17 degrees and a recoil arm at 68 degrees. A proton is said to be scattered left (right) if both counters in the left (right) forward arm fire in coincidence with both counters in the right (left) recoil arm. The positions of these arms guarantee that these events correspond primarily to proton-proton elastic scattering with a small contribution from quasielastic scattering off carbon. This reaction is chosen because it has a very large analyzing power. Even with the contamination from quasielastic scattering, the effective analyzing power at 800 MeV is A = 0.473. This number is taken from reference 14 and is their value for the line B polarimeter which is very similar to the polarimeter in line C.

The N-component of beam polarization, p_N, is calculated from the left-right asymmetry

$$p_N = \frac{1}{A} \frac{L - R}{L + R} .$$

Here L can be defined as the number of left scattered events and R as the number scattered to the right. However, this asymmetry will be skewed if the angular acceptance of the left and and right arms are different. This may occur if the counters are not placed symmetrically or, more commonly, if the beam is not symmetric or centered on the polarimeter target. The precision of the measurement can be much higher if we combine data taken with normal and reverse beams and assume that the polarization magnitude was the same for both states. Because left scattering with a normal beam is the same as right scattering with a reverse beam, we define L to be the geometric mean of the number of left scattered normal events and right scattered reverse events. Similarly, R is defined as the geometrical mean of the numbers of right normal and left reverse events. With these definitions, errors associated with instrumental asymmetries cancel to high order.

The S-component of beam polarization is measured with an identical arrangement of counters in the vertical plane containing the beam. Left and right in the above discussion are simply replaced by down and up. It is not possible to directly measure the L-component of polarization with such a polarimeter.

The statistical uncertainty in the measurement of each component of the beam polarization was obtained by assigning a $\sqrt{N}$ uncertainty to the number of counts for each event type (left-normal, left-reverse, right-normal, ...). An additional uncertainty of 0.01 was added in

quadrature to each measurement to account for residual errors due to instrumental asymmetries.

Each of the ratios r_S and r_N was assigned a single value for each of the three orientations of the beam polarization. Each value was calculated by taking a weighted average of all measurements and its uncertainty was obtained by combining the standard deviation of this average with the uncertainty arising from a ±1.0 degree fluctuation in the direction. The size of this fluctuation and the additional uncertainties assigned to the polarimeter and quench measurements were chosen to be consistent with the observed fluctuations in these ratios. The final values for the ratios r_N and r_S were -0.022 ± 0.019 and 0.874 ± 0.010 for the first beam orientation, 0.761 ± 0.014 and 0.010 ± 0.019 for the second, and -0.743 ± 0.013 and -0.010 ± 0.018 for the last. Figures 1-3 show these values and the data used to calculate them for each orientation of the beam polarization. The error bars on the points in these plots include only the statistical uncertainties.

The precession angle θ_p and the out of plane angle θ_o were calculated with a program which tracks protons through the magnet and calculates their spin precession. The program is based on the field map which accompanies the magnet and is described in appendix C. The precession angle was 13.8 degrees and the out of plane angle varied from 2.6 to 2.7 degrees.

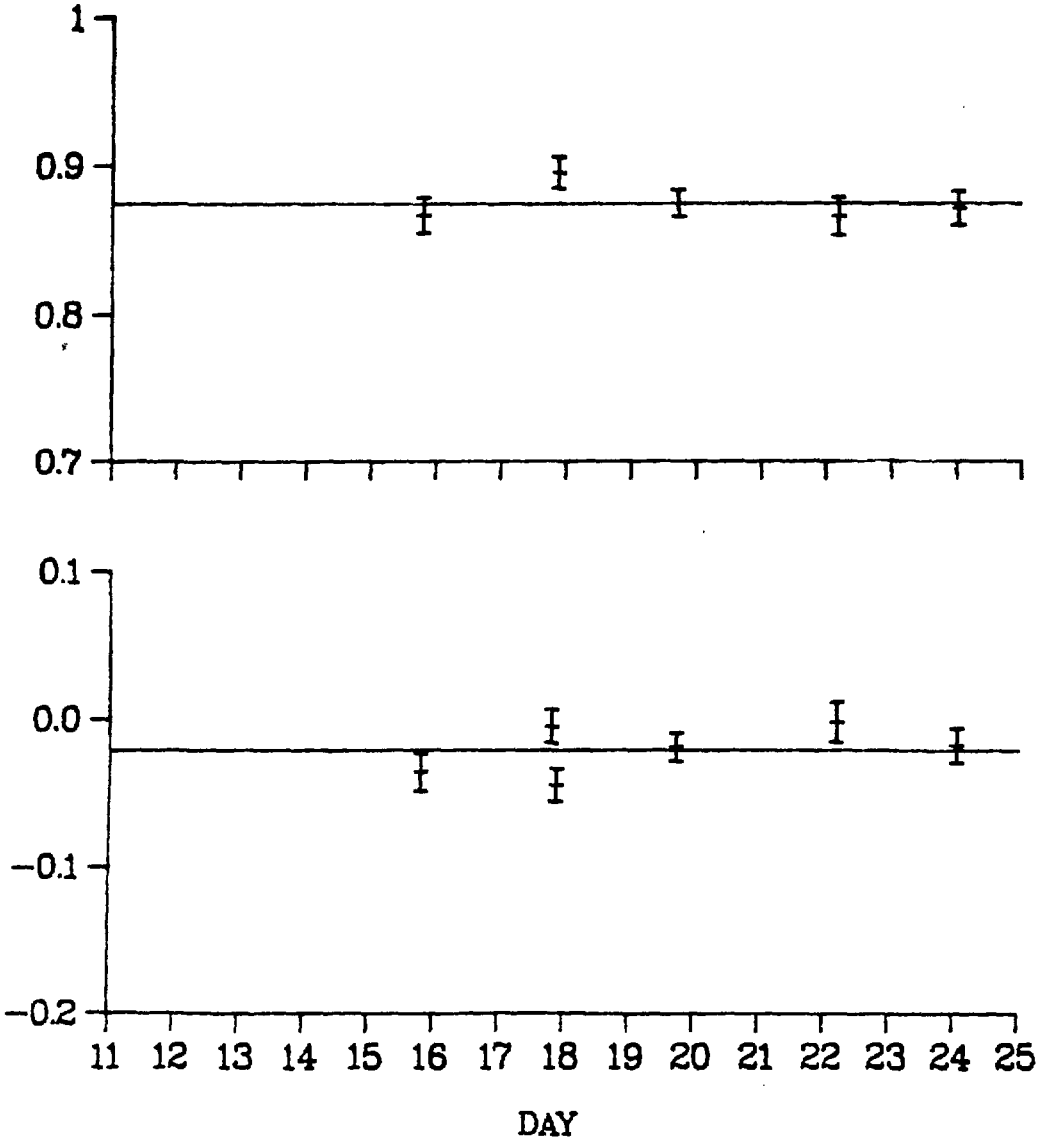

Figure IV-1

LCPO ratios p_S/p (top) and p_N/p (bottom) for the first orientation of the beam polarization.

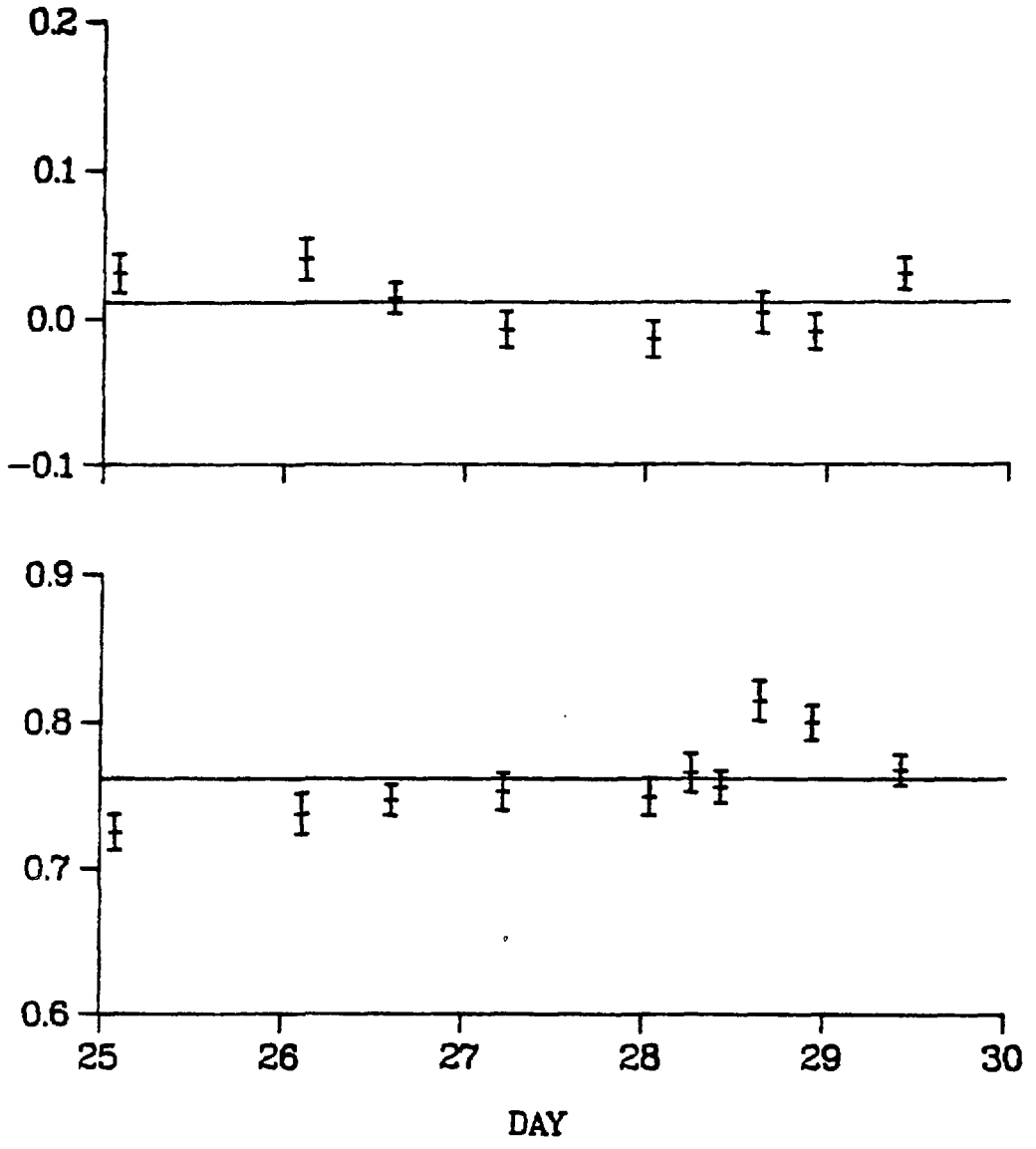

Figure IV-2

LCPO ratios p_S/p (top) and p_N/p (bottom) for the second orientation of the beam polarization.

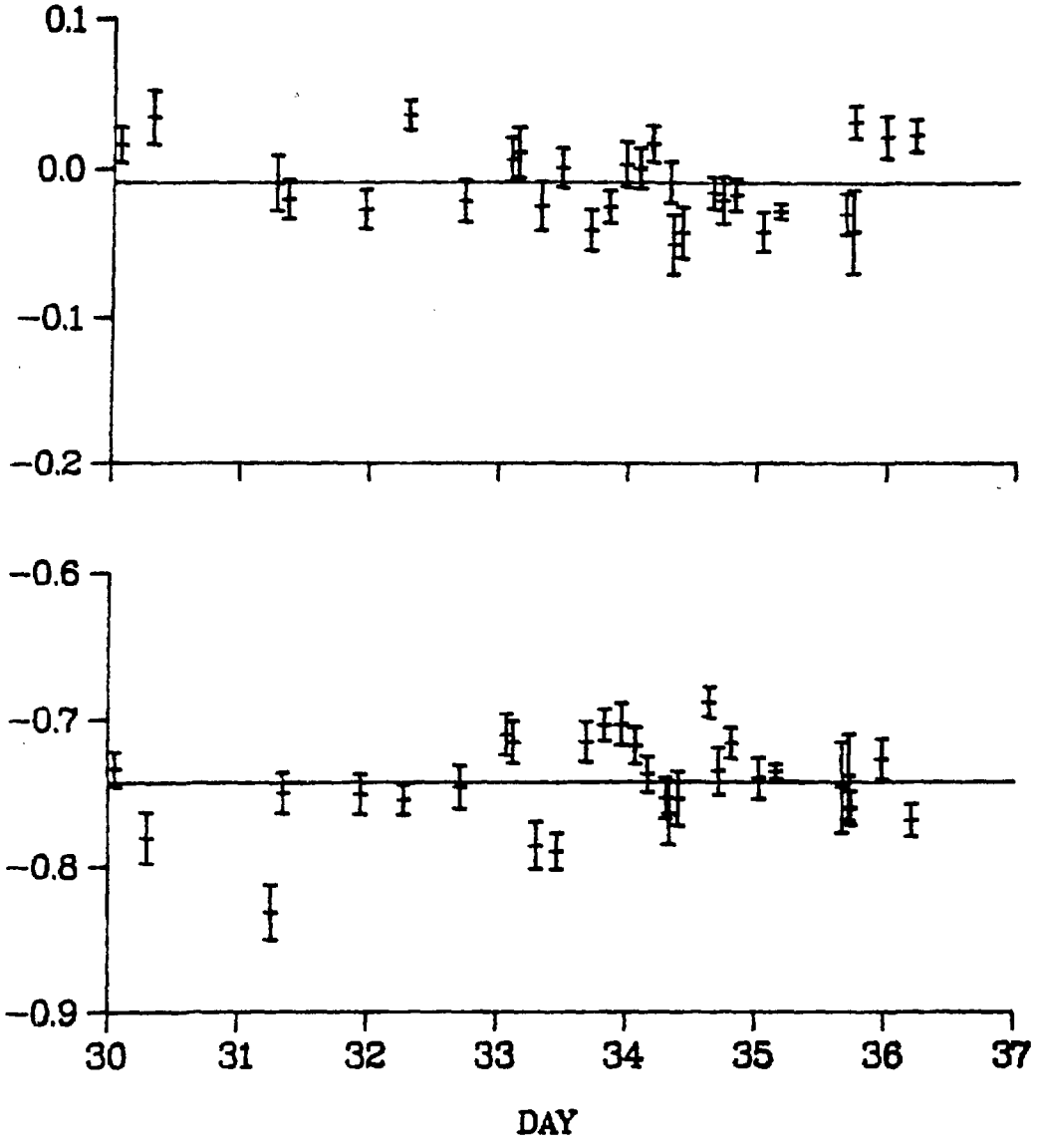

Figure IV-3

LCPO ratios p_S/p (top) and p_N/p (bottom) for the last orientation of the beam polarization.

V. Target Polarization

The deuteron target was repolarized every one to four days either because we needed to reverse the direction of the polarization or because significant depolarization had occurred. The polarization of the target was measured with a DMR (deuteron magnetic resonance) signal immediately after each polarization and immediately before repolarizing. In two cases a measurement was also taken in between and in two other cases a power failure caused a sudden depolarization of the target precluding the measurement before repolarizing. Regular measurements of the asymmetry in backward proton-deuteron elastic scattering were also made to monitor the relative target polarization. These asymmetry measurements were not very precise because of the low counting rate.

DMR Measurements

The deuteron has three magnetic substates because it is a spin one particle. We quantize along the field direction ($\hat{L}$). These states are labelled by the magnetic quantum number m which takes on the values +1, 0, and -1 in order of increasing energy. For a free deuteron in a field of 25 kgauss, the energy separation between the $m = +1$ and $m = 0$ states is the same as that between the $m = 0$ and $m = -1$ states and corresponds to the resonance frequency of 16.34 MHz. Denote the relative populations of these states by n_+, n_0, and n_- ($n_+ + n_0 + n_- = 1$).

The DMR signals provide a measurement of these relative populations which can then be used to calculate the target polarization. The populations are the expectation values of the corresponding projection operators which can be constructed from the spin operators J_L and J_{LL}:

$$\pi_+ = \frac{1}{2}(1 + J_L) J_L = \frac{1}{3} + \frac{1}{2} J_L + \frac{1}{6} J_{LL}$$

$$\pi_- = -\frac{1}{2}(1 - J_L) J_L = \frac{1}{3} - \frac{1}{2} J_L + \frac{1}{6} J_{LL}$$

$$\pi_o = 1 - J_L^2 = \frac{1}{3} - \frac{1}{3} J_{LL} .$$

We can invert these expressions and take expectation values to express the vector and tensor components of polarization in terms of the relative populations:

$$P = \langle J_L \rangle = n_+ - n_-$$

$$P_T = \langle J_{LL} \rangle = 1 - 3 n_o .$$

The DMR signal we measure is the absorbtion near the resonance frequency and it includes transitions between m = +1 and m = 0 states as well as those between m = 0 and m = -1 states. The strength of the DMR signal is proportional to $n_+ - n_o$ in the former case and to $n_o - n_-$ in the latter. The total area under the signal is the sum of these and is proportional to $n_+ - n_-$ and hence is proportional to the vector polarization. These areas were measured for all signals. The constant of proportionality when the target was polarized parallel to

the field was found to be different than that for the antiparallel configuration. It is possible to determine the absolute polarization if we separately measure the strengths of both transitions and make one assumption about the relative populations of the states.

The assumption we make is that of equal spin temperatures. The validity of this assumption is discussed in reference 15. We assume that the populations of the spin states follow a Boltzmann distribution which implies that the ratios n_+/n_0 and n_0/n_- are equal. Denote this common ratio by r. The ratio of the strength of the $m = +1$ to $m = 0$ and the $m = 0$ to $m = -1$ transitions provides a direct measure of this ratio because

$$\frac{I_{+0}}{I_{0-}} = \frac{n_+ - n_0}{n_0 - n_-} = \frac{r - 1}{1 - 1/r} = r \ .$$

It is possible to measure the ratio of transitions because the quadrupole moment of the deuteron interacts with the electric field gradient of the propanediol molecule. This leads to a splitting of the two transitions although the two peaks are not completely resolved because the molecules are oriented isotropically. The complicated fitting of this signal is discussed in reference 16. Figure 1 shows a typical example of the signal and the fit.

The vector and tensor components of polarization can be expressed in terms of the ratio r:

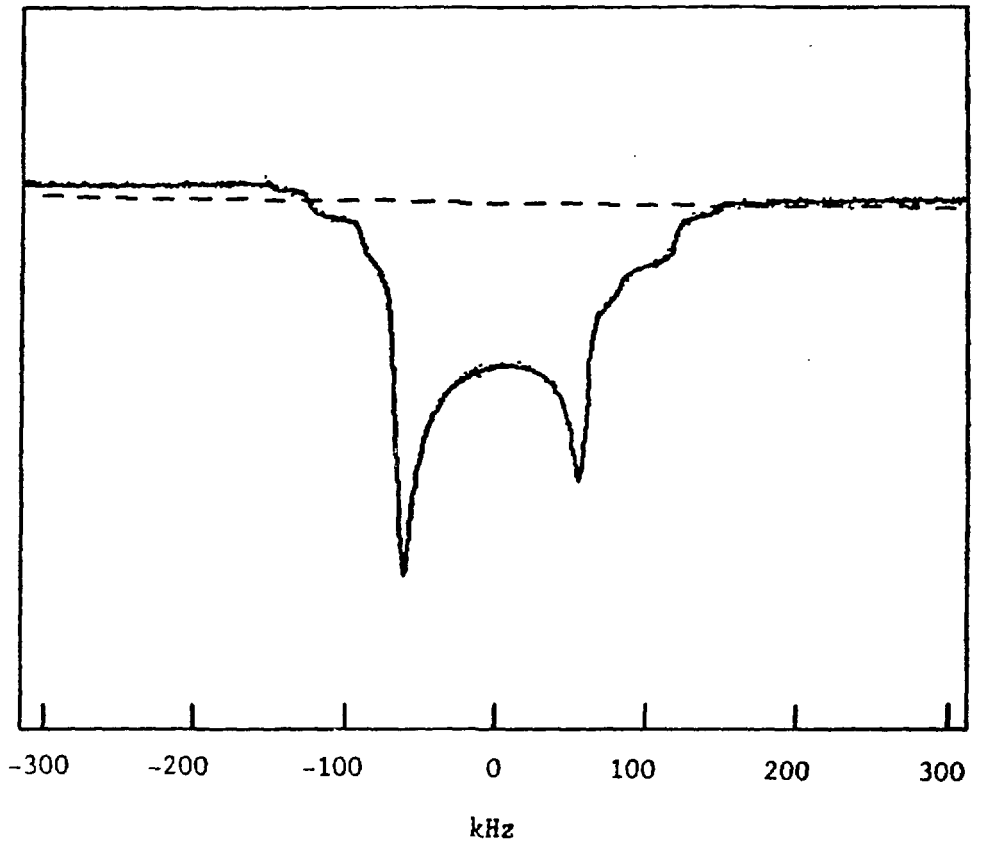

Figure V-1

Typical DMR signal (points) and the fit (solid line) used to measure the absolute target polarization. The dashed line is the voltage measured without the DMR signal.

$$P = \frac{r^2 - 1}{r^2 + r + 1}$$

$$P_T = \frac{r^2 - 2r + 1}{r^2 + r + 1} .$$

Most of the DMR signals were fit to calculate the absolute polarization. The ratio between the absolute vector polarization and the signal area was determined by averaging over all such runs. This was done separately for runs with the target polarized parallel to the field and those with the polarization antiparallel to the field direction. The parallel ratio was found to be 0.626 ± 0.7% and the antiparallel was 0.670 ± 0.4%. The values assigned for the target polarization were obtained by multiplying the measured areas by these factors. The estimated uncertainty in the measurements is 0.01. Table 1 and figure 2 present the values.

Because the target polarization was observed to decrease between DMR measurements, it was necessary to interpolate between these values to obtain the target polarization for each series of runs. The bulk of the observed depolarization was assumed to take place during the periods of highest beam intensity. Because the largest polarization decrease between DMR measurements was only 0.03, an independent uncertainty of 0.01 was assigned to the target polarization for each series.

Date	Hour	P	Date	Hour	P
Aug 11	11:15	0.235	Aug 25	19:30	0.261
13	15:00	0.228	26	22:10	0.256
			27	15:15	0.252
14	19:55	-0.324			
16	16:20	-0.317	27	17:45	-0.337
19	7:25	-0.304	29	15:20	-0.326
19	8:45	-0.337	29	19:00	0.245
20	12:30	-0.327	30	9:10	0.239
20	18:20	0.254	30	21:30	0.261
			Sep 1	4:30	0.244
21	20:40	0.250			
23	6:00	0.219	1	7:50	-0.331
			2	14:45	-0.326
23	11:45	0.239			
24	20:10	0.209	4	14:00	-0.380
			5	8:50	-0.373
24	22:20	0.266			

Table 1

Measurements of the vector polarization of the target ($\hat{L}$ direction). The blank lines indicate a repolarization of the target.

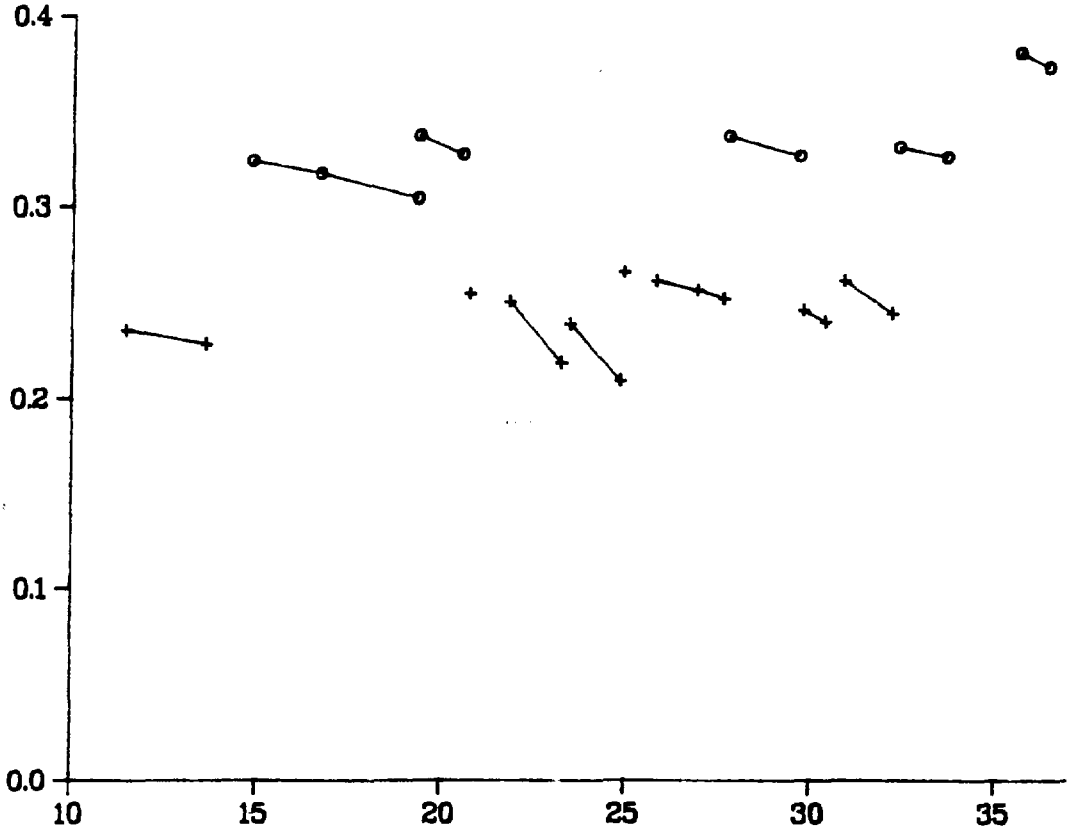

Figure V-2

DMR measurements of the vector polarization of the target. The points indicated with crosses were taken with the polarization parallel to the magnetic field ($\hat{L}$ direction) and the circles in the antiparallel configuration. The horizontal axis is the day.

Backward Scattering Asymmetries

The asymmetry at 180 degrees is proportional to the target polarization and was measured regularly to monitor the relative polarization. Our measurements of this asymmetry and the extraction of the analyzing power A_{LL} are discussed in appendix D. The reduced chi squares for the fits used to calculate the analyzing power were around 0.5 indicating that the asymmetry measurements are in good agreement with the DMR results. However, this is only a rough check because the uncertainties in these asymmetries are between 10 and 20% while the DMR measurements are estimated to be good to 3 or 4%.

These asymmetries were also used to provide a check of the relative normalization between the two orientations of the target polarization. A ratio was formed between the values of A_{LL} obtained from runs taken with the target parallel to the beam and those taken in the antiparallel configuration. The value of A_{OLL} (see appendix D) was fixed at values from -1.0 to 1.0 and this ratio varied from 1.10 to 1.05 with an uncertainty of 0.09. Thus, the relative value of the DMR normalization between the two target orientations is confirmed at a level of about 8%.

VI. Data Reduction

The first step in calculating the asymmetries and outgoing polarizations is to use the data written to tape to construct the required histograms and focal plane polarimeter (FPP) sums. This procedure is referred to as the replay of the data. The chamber calibration procedure described below is used to determine the parameters needed to calculate focal plane trajectories from the raw data. These trajectories are then used to calculate kinematic variables describing the scattering at the target and in the carbon. Each event is subjected to to series of tests and those events passing certain tests are included in the histograms or FPP sums.

Chamber Calibration

All of the cathode wires in each plane end at a common delay line and the signal induced by a charged particle travels down the nearest cathode wire to this line. The difference between the times required for the signal to travel to the two ends of the delay line is measured by a TDC which is started by the signal from one end and stopped by the other. Another TDC is started by the trigger and stopped by the signal from one of the two ends of the delay line. The information from this TDC is combined from with that from the first to calculate the average of the times required for the signal to reach each end.

The time difference is used to determine which wire was nearest the particle trajectory. Ideally, this time difference should be quantized with each wire always producing the same value. The difference in time for two different wires is twice the time required for the signal to travel along the delay line by the distance separating the wires. In practice, jitters in the electronics spread out the distribution of times for a given wire but adjacent wires are generally well resolved. The wire number for each event is obtained by truncating a second order polynomial function of the time difference. Figure 1 shows an example of this polynomial superimposed on the truncated polynomial. The constants which appear in this polynomial function are determined by comparing the raw and truncated polynomial spectra.

The average time is, up to an additive constant, just the time required for the signal to drift to the wire (drift time) and is used to determine the drift position (the distance from the wire). The drift position is assumed to be a monotonic function of the drift time and a calibration is made so that the spectrum of drift positions for each wire is constant between zero and half a wire spacing and vanishes elsewhere. Figure 2 shows a typical drift time spectrum and the corresponding drift position spectrum. The first set of chamber tests are applied to the drift times.

Knowledge of the wire number and drift position does not completely determine the position at the plane because we must still resolve the left-right ambiguity; i.e., we must determine on which

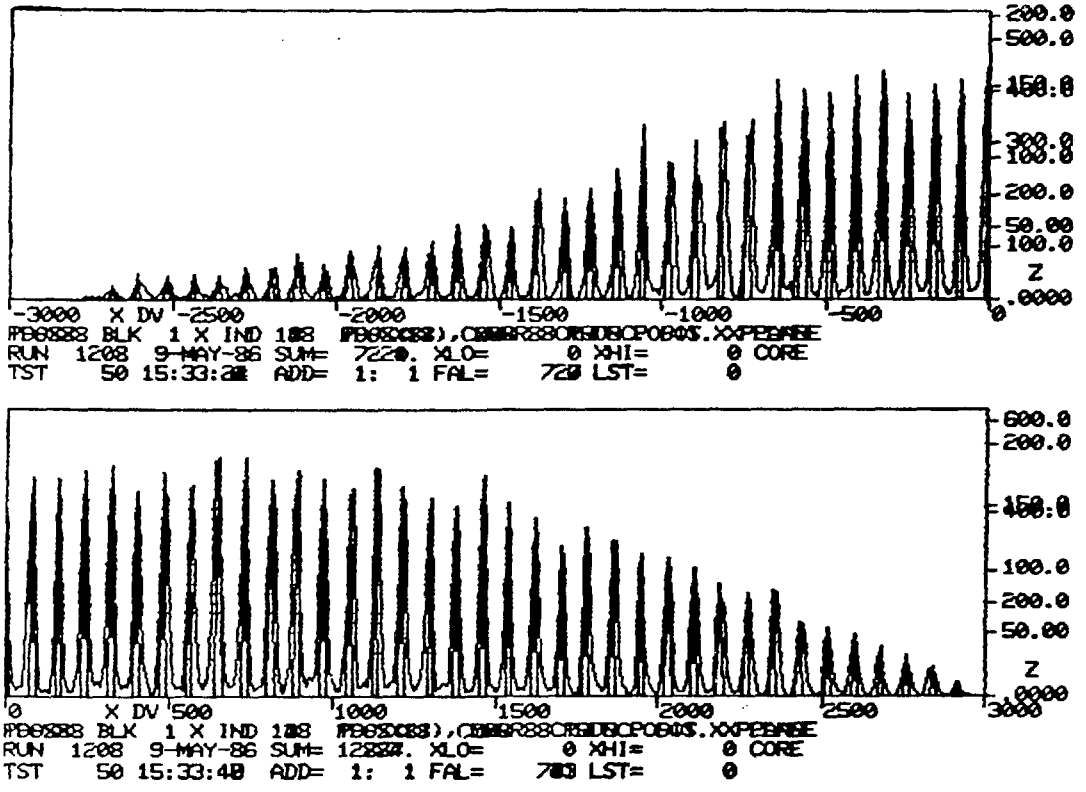

Figure VI-1

Polynomial function of the time differences superimposed on the truncated polynomial used to make wire number assignments. Units are 0.01 cm.

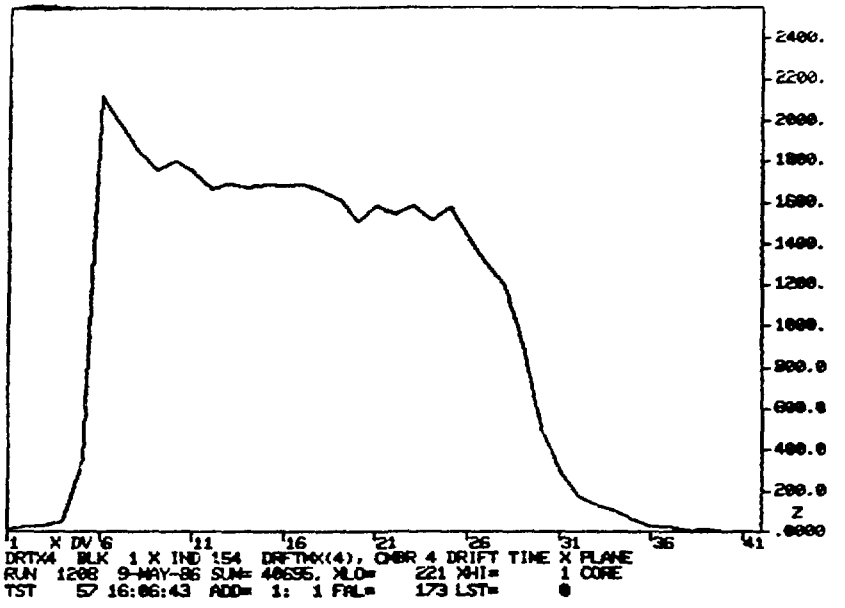

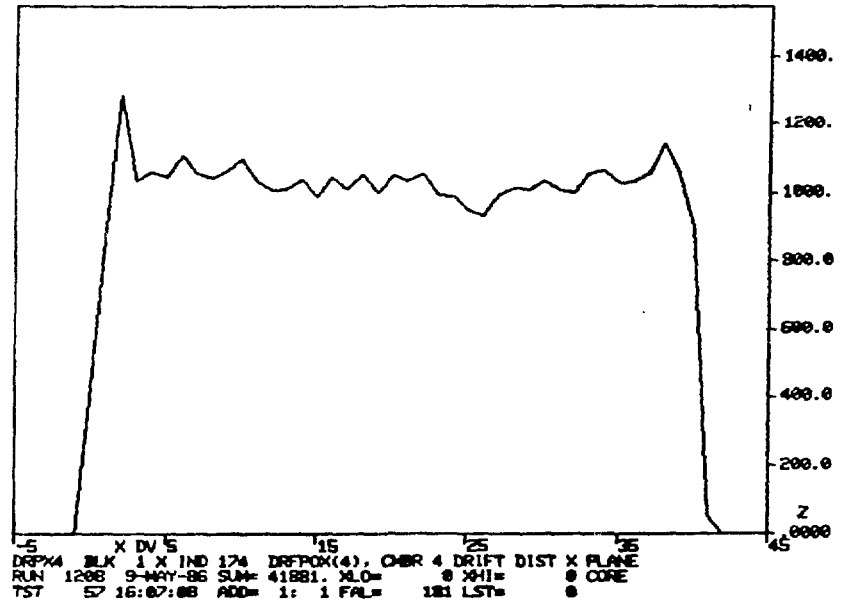

Figure VI-2

Drift time (top) and corresponding drift position (bottom) spectra. The units for the bottom figure are 0.01 cm.

side of the wire the particle passed. This ambiguity is resolved by comparing the two planes in a pair (i.e., the two planes within a chamber which have the same orientation but are offset by half a wire spacing). The two possible positions in one plane and the two in the second are combined with a rough calculation of the trajectory and the ambiguity is resolved by choosing those positions which give the best fit to a straight line trajectory.

The calibrations discussed above determine the particle position at each plane up to an additive offset. The difference between the offsets for the planes within a pair is determined by comparing the calculated positions in the two planes. A rough calculation of the trajectory is used to predict the difference between these positions. The difference between the predicted and observed differences is calculated on an event by event basis and the offsets are adjusted so that this difference averages to zero. Figure 3 shows a typical spectrum of this difference. The small peak near channel 80 is one wire spacing from the origin and is presumably due to wire misidentification. The second set of chamber tests are applied to these differences.

The average offsets for each of the pairs of planes in the front chambers were determined by taking a run without a target with the spectrometer set at zero degrees and the magnets set for the beam energy. The front chamber information determines the missing mass, horizontal and vertical scattering angles, and the y position at the target. For this spectrometer setting, all these should average to

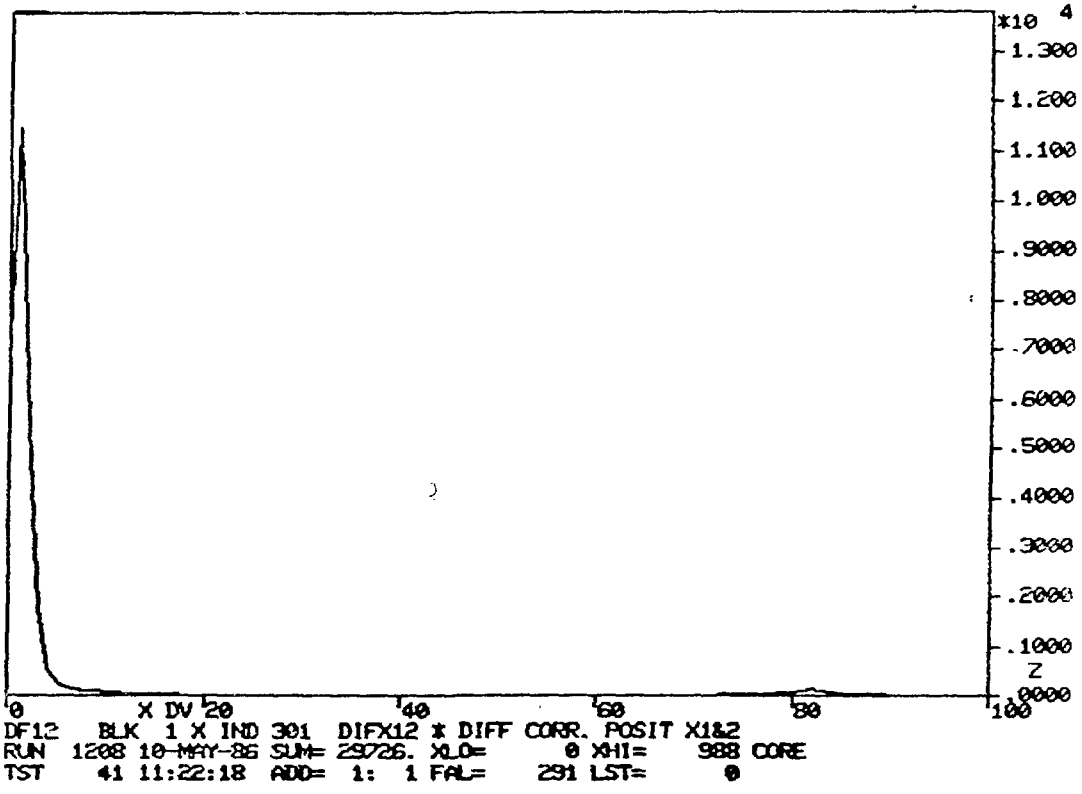

Figure VI-3

Difference between the positions calculated in each of two paired planes corrected for the difference expected from the trajectory. Units are 0.01 cm.

zero and the front chamber offsets were adjusted accordingly before the replay of the FPP data.

These average offsets were not adjusted carefully for the replay of the asymmetry data. This resulted in unimportant offsets in the calculation of the missing mass and the y position at the target and in offsets of 0.65 and 0.16 degrees in the calculations of the vertical and horizontal scattering angles at the target. The angular offsets cause negligible decreases in the resolution of the scattering angle and missing mass. The only noticeable effect is an offset of less than 0.2 degrees in the calculation of the scattering angle. Typical distributions of scattering angles calculated for both asymmetry and FPP data are shown in figure 4.

Because the zero degree run was taken without the carbon blocks, the trajectory calculated from the front chambers could be used to predict the positions at the rear chambers. These predicted positions were then used to determine average offsets for the rear chambers pairs. However, the polarization measured at the focal plane is very sensitive to the values of the rear chamber offsets relative to those of the front chambers. For this reason, the average offsets for each of the rear chamber pairs were checked on a run by run basis and adjusted where necessary. This was accomplished using those events which were not tested in the MBD. These events almost all have a very small scattering angle in the carbon and their average analyzing power is therefore also quite small.

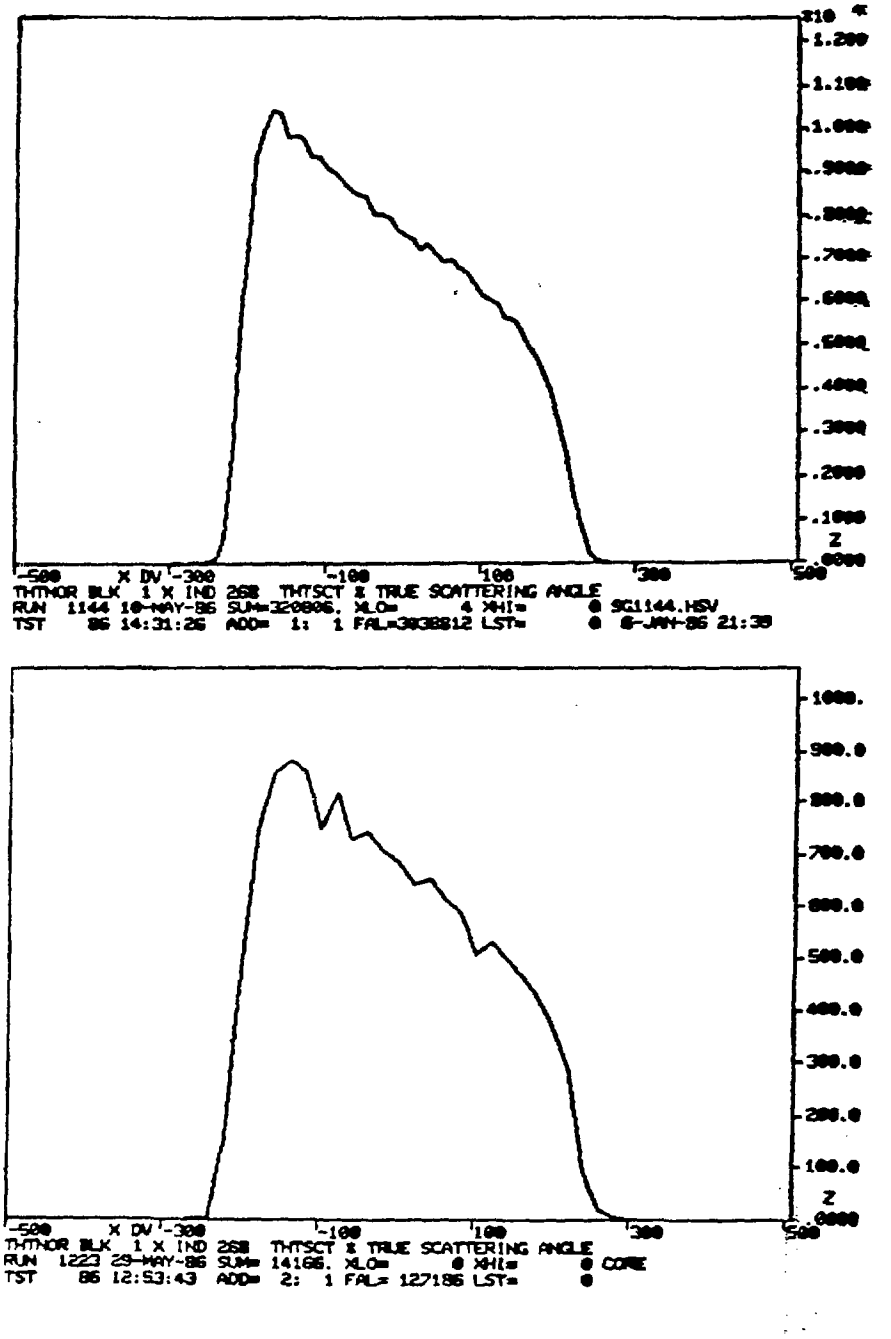

Figure VI-4

Typical distributions of scattering angles calculated with asymmetry data at 16.5 degrees (top) and FPP data at 14 degrees (bottom). Units are 0.1 mrad and the origin corresponds to the spectrometer setting.

Event Tests

The events on tape are subjected to a number of tests to determine whether they should be included in the histograms or FPP sums. Two types of tests were used – gates and boxes. An event passes a gate test if the value of the tested variable falls within certain limits. A box is the same as two gates and each of two variables must fall between certain limits for the test to be passed.

All events are first subjected to a particle identification (PID) test which is composed of two boxes. Both boxes include the pulse height in scintillator S1 which is defined as the mean output from the ADC's attached to the phototubes above and below the scintillator. The other variable for the first box is the time of flight from S1 to SP1 and for the second box is the time of flight from S1 to SP2. An event passes the PID test if it passes either one of these box tests. We chose the limits for the boxes to be quite wide because there was no evidence for anything except protons. More than 99% of all events pass this test. Typical boxes are shown in the scatter plots in figure 5 where each point corresponds to an event.

The variables used for the two sets of chamber tests have already been described. The gates on the drift time spectra were set at channels 1 and 45 (see the top of figure 2) and the gates on the difference spectra (figure 3) were set to reject all events outside 2 mm (20 channels). Between 20 and 25% of the events failed at least

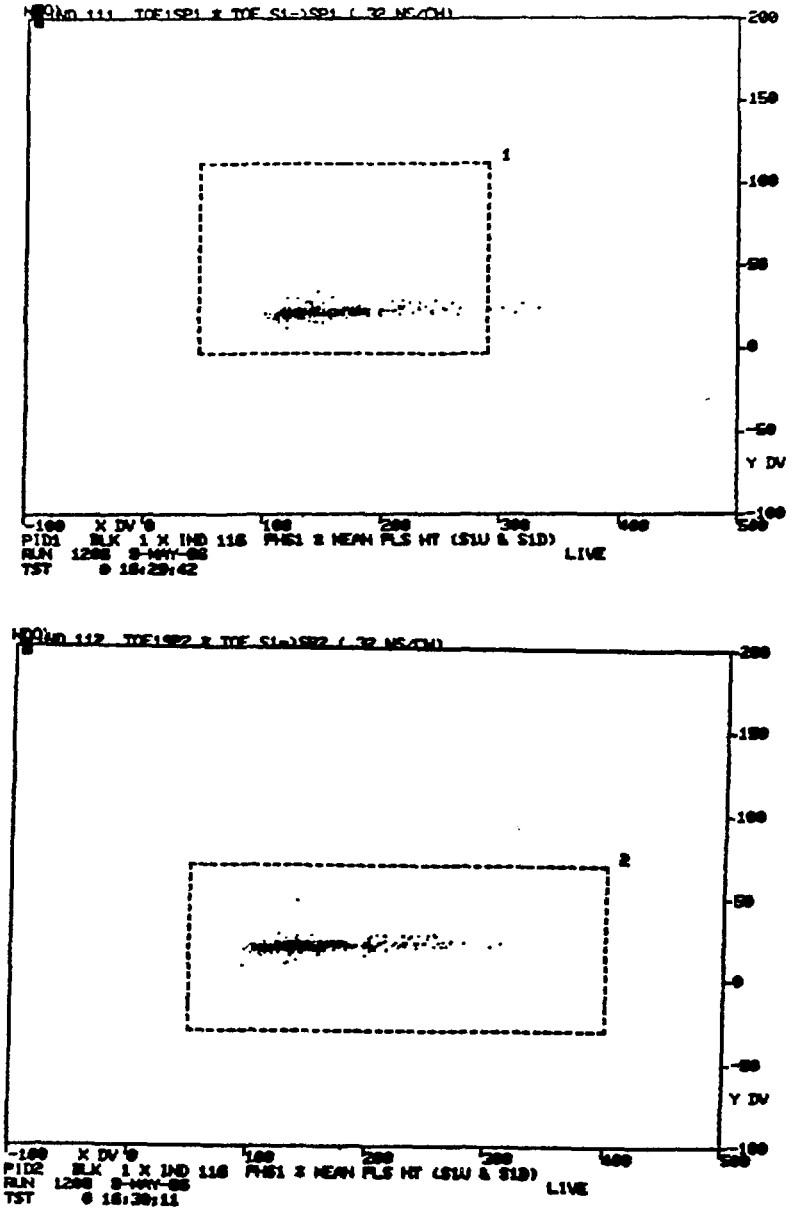

Figure VI-5

PID boxes. The vertical axis is the time of flight from S1 to SP1 (top) or SP2 (bottom) and the horizontal axis is the pulse height in S1.

one of the front chamber tests and 45 to 50% failed one or more of all chamber tests.

Another standard box test is XANG. Here one variable is the vertical position at the focal plane and the limits were chosen to be larger than the physical acceptance. The extreme values for the second variable, THTCUT, occur when particles are near the limits of the spectrometer acceptance. Between 20 and 30% of all events failed this test. A scatter plot of these variables and the XANG box are shown in figure 6. The distribution of vertical positions in this figure is limited because the data was taken with SX in the trigger.

The scattering angle at the target was subjected to a gate test. The histograms in figure 4 include events which passed all front chamber tests and which have a missing mass in the region corresponding to proton-deuteron elastic scattering. The same gate was used for both asymmetry and FPP data and the limits were set at channels -200 and 250 so that very few events were rejected in either case.

A gate was set on the missing mass to maximize the number of events corresponding to proton-deuteron elastic scattering while minimizing contributions from the background and especially the breakup and helium peaks. Different limits were used for each angle but the same limits were used for all runs at a given angle. The gates are shown in figures 1-4 in chapter VII and are discussed in appendix A.

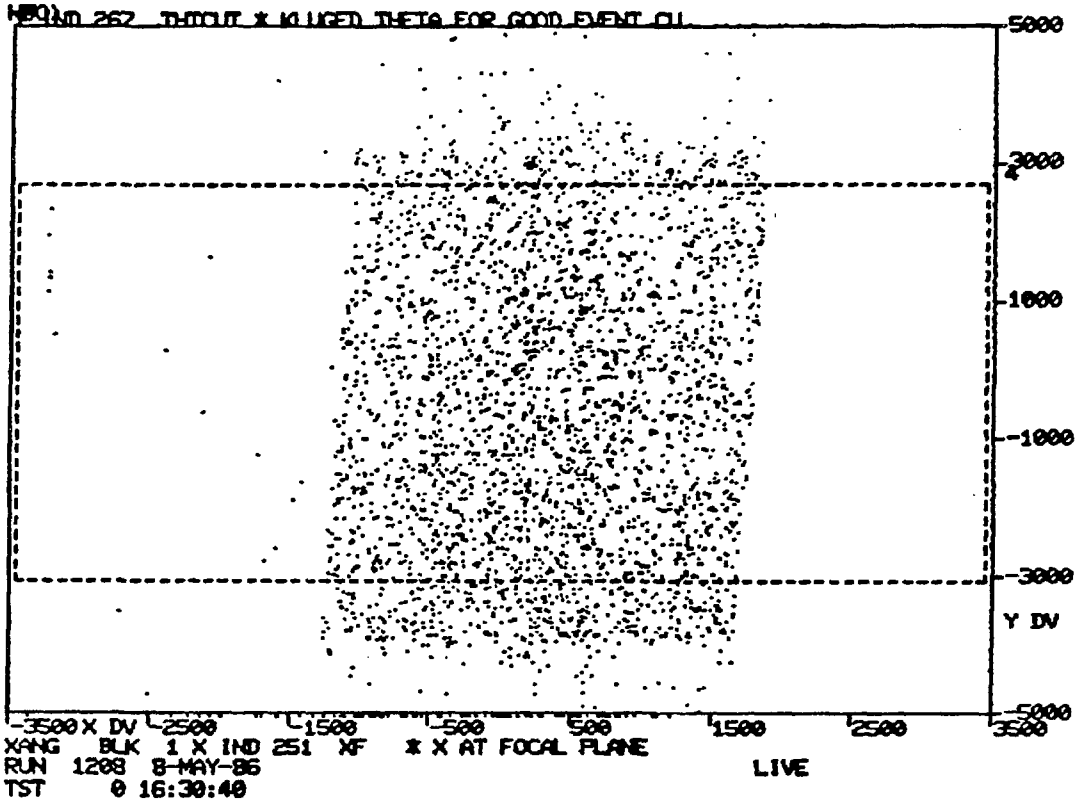

Figure VI-6

XANG plot. The vertical axis is the composite variable THTCUT and the horizontal axis is the vertical position at the focal plane. Units on the horizontal axis are 0.01 cm.

The polar scattering angle in the carbon was also subjected to a gate test with limits 4.5 and 20.5 degrees. The analyzing power of the carbon is well known and relatively large in this region. It is important that the on line cut in the MBD be outside this region because it is not necessarily symmetric and could introduce a false asymmetry. Figure 7 shows the distribution of carbon scattering angles without the MBD cut and the distribution actually written to tape which for which about 95% of the events were tested in the MBD. The spectrum without this cut rises sharply at small angles but there is very good agreement between the two spectra within the gated region between channels 785 and 3578.

The carbon block test is a box which checks the point of closest approach of the trajectories calculated from the front and rear chambers. One variable is the distance between the two trajectories at closest approach and the limits were chosen to be 0 and 1.9 cm. The other variable is the z position at closest approach where z is the direction normal to the chambers. The limits for this latter variable were chosen so that only those events which appeared to scatter in the carbon were accepted. A scatter plot of these variables and the box are shown in figure 8.

The events used to construct the missing mass histograms (i.e., those used to calculate the asymmetries) were required to pass all front chamber tests as well as the XANG, PID, and scattering angle tests. The events used in the FPP sums (i.e., those used to calculate the focal plane polarization) were required to pass all these tests as

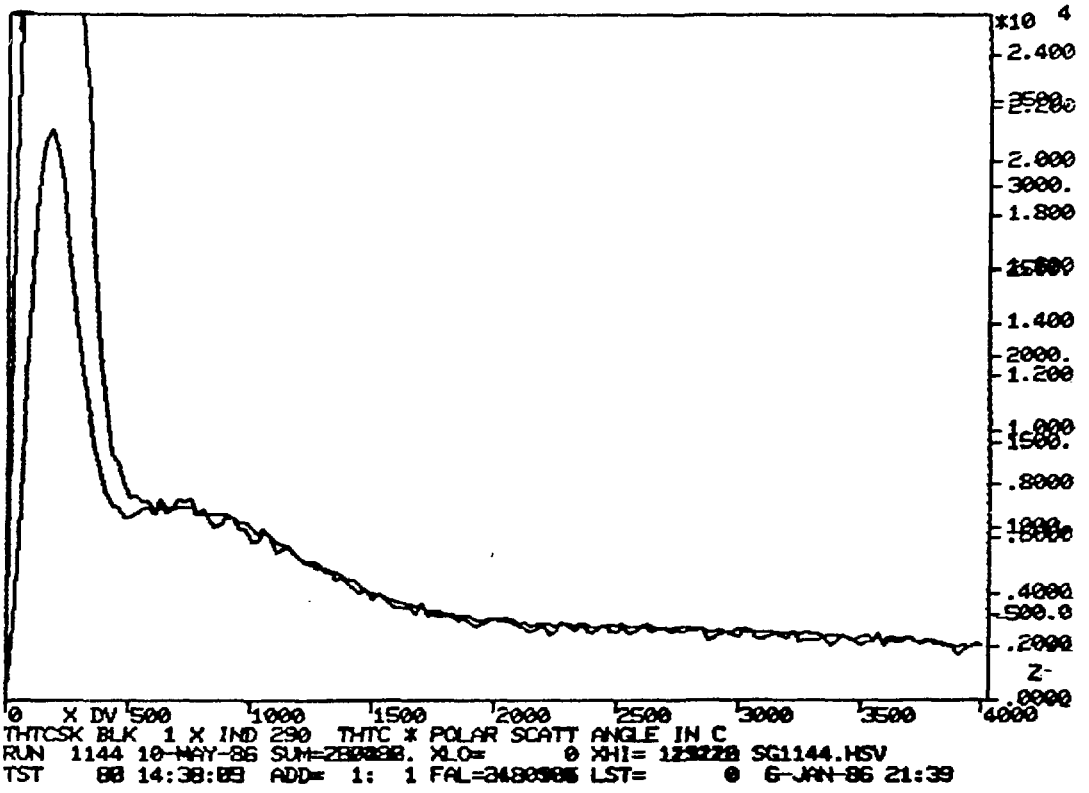

Figure VI-7

Carbon scattering angle distribution written to tape and that without the MBD cut. Units are 0.1 mrad.

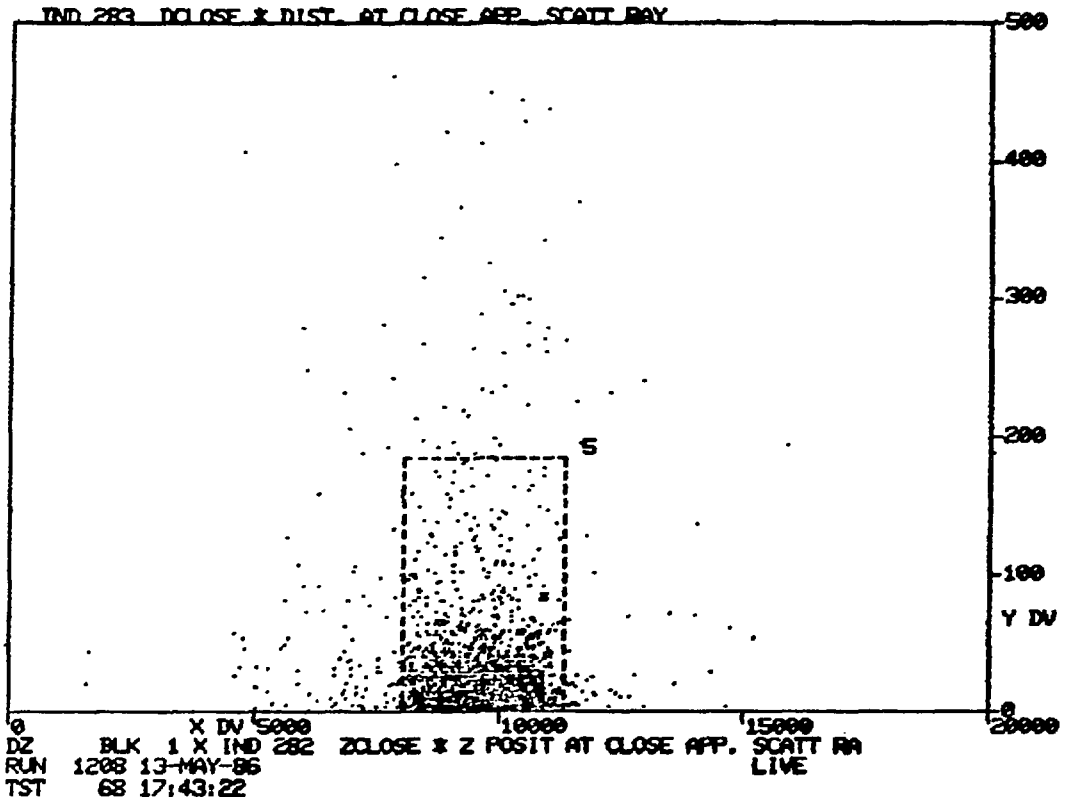

Figure VI-8

Carbon block box. The vertical axis is the distance at closest approach and the horizontal axis is the corresponding z position. The units on both axis are 0.01 cm.

well as all rear chamber tests, the missing mass test, the carbon scattering angle test, and the carbon block test. The FPP events were also required to pass the $\phi + \pi$ test discussed in chapter VIII.

VII. Asymmetries

The asymmetry resulting from the beam polarization is defined as the ratio between the difference and sum of the relative yields in the normal and reverse beam polarization states:

$$\varepsilon = \frac{Y_{nor} - Y_{rev}}{Y_{nor} + Y_{rev}} .$$

The relative yield was obtained by counting the number of proton-deuteron elastic scattering events and dividing by the relative integrated beam intensity, the computer live time, and the chamber efficiency. The uncertainty in each asymmetry was calculated from the error in the estimate of the number of elastic events. Uncertainties in the beam intensity, computer live time, and chamber efficiency are all much smaller and have been neglected.

The computer live time was obtained by dividing the the number of triggers counted while the computer was available for data taking by the total number received. These were scaled and calculated separately for normal and reverse beam.

The chamber efficiency was calculated separately for normal and reverse beam using events which passed the particle identification test. The efficiency is the fraction of such events which passed all front chamber tests.

The relative normal and reverse beam intensities were obtained from appropriately gated scalars which read the integrated output of the ion chambers behind the target.

The number of proton-deuteron elastic events was obtained by fitting missing mass (excitation energy) histograms which were compiled during the replay of the data. The fitting was done using a modified version of the MIT computer code ALLFIT. This code uses parameterized backgrounds and peaks to create a fit to the data by finding those values of the parameters which minimize a chi-square function. The chi-square function used is that appropriate to Poisson statistics.

At all angles, the spectra were assumed to consist of a deuteron elastic peak, a deuteron breakup peak, and a continuous background. At 7 and 11 degrees, ^{3}He and ^{4}He elastic peaks were also included. The helium contributions were handled separately because the relative levels of ^{3}He and ^{4}He could change from run to run. For each series of runs corresponding to a particular scattering angle and orientation of the beam and target polarizations, the normal and reverse spectra were fit simultaneously; i.e., the code minimized a single chi-square function describing both spectra. The shape and position of each peak were required to be the same on the two spectra while the heights were allowed to vary independently. Separate backgrounds were constructed for each spectrum as described below. The asymmetry and its uncertainty were then calculated using the the final values and

(correlated) uncertainties of the parameters describing the proton-deuteron elastic peaks.

Peak Parameterization

The deuteron elastic peak was described with the hypergaussian function,

$$y(E) = H \exp\left[-\left(\frac{|E-E_0|}{k_r w(1\pm\alpha)}\right)^r\right] .$$

Here H is the peak height, E_0 and w are the peak position and width (FWHM) in MeV, and r and α are dimensionless shape parameters. The sign preceeding α is negative for $E < E_0$ and positive for $E > E_0$ and $k_r = .5(\ln 2)^{-1/r}$. The peak height was allowed to vary independently on the two spectra. The position, width, and other shape parameters were each allowed to vary but were required to have the same value on normal and reverse spectra. The shape of this peak was used as a resolution function for other peaks in the spectrum; i.e., other peaks were assigned intrinsic shapes which they would have had if the energy resolution had been arbitrarily high and these shapes were folded with the resolution function to obtain the final peak shapes.

The deuteron breakup peak was described by folding the resolution function with a broad Lorentzian distribution

$$y(E) = \frac{H(E-T)^2 w^2}{[(E-T)^2+(E_0-T)^2]^2 + (E-T)^2 w^2} \qquad E > T$$

$$= 0 \qquad E < T \ .$$

The peak height, H, was allowed to vary independently on both spectra but the width, w, was fixed and the position, E_0, and threshold, T, were fixed relative to the deuteron elastic peak. The fixed parameters were determined by fitting HRS spectra taken with a liquid deuterium target in another HRS experiment.[10] These spectra had much better resolution and almost no background. The width used was 20 MeV and the position was taken 2 MeV above the threshold. The threshold relative to the deuteron elastic peak was 2.1 MeV at 7 and 11 degrees and 2.4 MeV at 14 and 16.5 degrees. In many cases, the position and threshold of the breakup spectra were shifted by about one MeV and the calculated asymmetry was found to change by an amount small compared to its uncertainty.

The missing mass calculated for elastic proton-helium scattering events depends on the scattering angle because the calculation is performed assuming proton-deuteron kinematics. The intrinsic helium elastic peak shapes and positions were obtained by assuming a uniform scattering angle acceptance between -1.0 and 1.0 degrees and weighting with the unpolarized cross section taken from reference 17. This intrinsic shape was then folded with the resolution function. At 7 degrees, where the helium makes a very important contribution, some of the runs were also fit assuming an acceptance between -0.8 and 0.8

degrees. The asymmetries did not change significantly. The heights of both peaks on both spectra were allowed to vary independently.

Background

The fixed background shapes were determined from runs taken at each angle with non-deuterated propanediol in a mock target. Protons scattered from the hydrogen (which replaces the deuterium in the real target) appear at an excitation energy above the fitting region. Because the amplitude and shape of this background can depend on the N-component of the beam polarization, the background spectra were taken with a beam which contained a large N-component and normal and reverse spectra were fit separately. Normal and reverse backgrounds were obtained at 14 and 16.5 degrees by fitting with a low order polynomial. At 7 and 11 degrees, the spectra were smoothed by averaging over adjacent channels. These normal and reverse backgrounds obtained from the mock target runs were then added with appropriate weighting to create separate normal and reverse backgrounds for each fit. Different weighting was used for different runs because the N-component of beam polarization varied from run to run.

Because the energy of the beam at the target could vary by a few MeV between runs, the position of the background was defined relative

to the proton-deuteron elastic peak. The same relative position was used for all fits at each angle.

The standard deuterated propanediol target was made up of closely packed solid spheres while the mock target consisted of liquid non-deuterated propanediol. Thus, we expect that the backgrounds determined with the mock target will have to multiplied by a factor of about 0.7. This factor is referred to as the background level. This level could only be determined by the region of the missing mass spectrum below the proton-deuteron elastic peak because the region above includes the breakup peak which overlapped the elastic peak.

At 14 and 16.5 degrees, the background position was determined by simultaneously fitting eight spectra with a single variable background position. The asymmetries were found to be insensitive to shifts of a few MeV in this position. This is not surprising because the 14 and 16.5 degree backgrounds are fairly linear functions of missing mass.

At 11 degrees, the background contains some structure and more precise positioning was required. This structure was obscured by the helium elastic lines in standard runs so the position was determined with a special run taken with the helium removed from the target. This run was fit with various background positions and the final position was taken to be that which gave the best fit, i.e. that with the smallest chi-square value. The measured asymmetry for this special run changed by only 0.002 when the position was increased or

decreased by two channels (0.4 MeV) while the chi-square increased from 170 to 210.

Below the proton-deuteron elastic peak at 7 degrees, the background increases very rapidly as the missing mass decreases. Because part of this increase is due to contributions from helium elastic scattering, a special run taken without helium was again used to determine the background position. The final position corresponded to a background level of 0.73 and a reduced chi-square of 1.19. A decrease of one channel in this relative position changed the level to 0.87 and chi-square to 1.10. Although the chi-square appears to represent an improvement, this level is unreasonably high. An increase of one channel in the background position yielded a background level of 0.61 and a chi-square of 1.57. This level is a little low and certainly the chi-square is much worse. The asymmetry for this run changed by less than 0.002 in both cases. All spectra were fit one channel above and one channel below the standard position and the average of these two changes was included in the uncertainty in the asymmetry. There was only one run where the average change was greater than 0.002.

The background level at 16.5 and 14 degrees was well determined by the data (see figures 1 and 2) but it was not possible to obtain good fits using the same background level for all runs. In the fits used to calculate the asymmetries, the background level was varied for each run but was required to have the same level on the normal and reverse spectra. The levels varied from 0.70 to 0.76 at 16.5 degrees

and from 0.66 to 0.73 at 14 degrees. Fits in which the normal and reverse levels were allowed to vary independently gave comparable fits to the data with slightly larger uncertainties in the calculated asymmetries.

At 11 degrees, the helium peaks begin to overlap the proton-deuteron elastic peak (figure 3) but, because their shapes are very different from that of the background, the background level and the peak heights were allowed to vary. The background level was required to be the same on both spectra and these levels varied from 0.59 to 0.65.

At seven degrees, there is considerable overlap between the helium and deuteron elastic peaks (figure 4) and the level was fixed at 0.7 on both normal and reverse spectra. Fits were also made with levels of 0.6 and 0.8 and the average change was included in the uncertainty. This average change was generally quite small – 0.002 or less in all but one case.

The variation of the background level from run to run indicates a change in either the normalization or the composition of the background. The normalization was checked by adding normal and reverse yields for each run. This sum should be fairly constant because parity guarantees that it cannot depend on the vector polarization of an L-type target and the tensor polarization is small and always in the same direction. This sum varies over a smaller range than the background level and is not strongly correlated. This

implies that variations in the normalization cannot explain the observed changes in the background level.

The composition of the background could change from run to run if it included significant contributions from helium or the walls of the cryostat. The helium level did vary from run to run and the observed background level may have included contributions from inelastic scattering or tails of the elastic peak. The higher background levels at 14 and 16.5 degrees support the idea of inelastic helium scattering because the thresholds for these reactions lie below the deuteron elastic peak only at these angles.

However, as the results at seven degrees indicate, the measured asymmetry is is not very sensitive to average background level. In order for these spurious background contributions to significantly alter our results, their analyzing power would have to vary dramatically with missing mass.

Results

The asymmetries and their uncertainties were taken to be those calculated with the fit code as described above except that the uncertainties at seven degrees were modified by adding in quadrature the changes obtained by varying the position and level of the background.

The reduced chi-squared values for the fits fell between 0.8 and 1.5. The magnitudes of the asymmetries ranged from 0.04 to 0.27 and their uncertainties from 0.005 to 0.012.

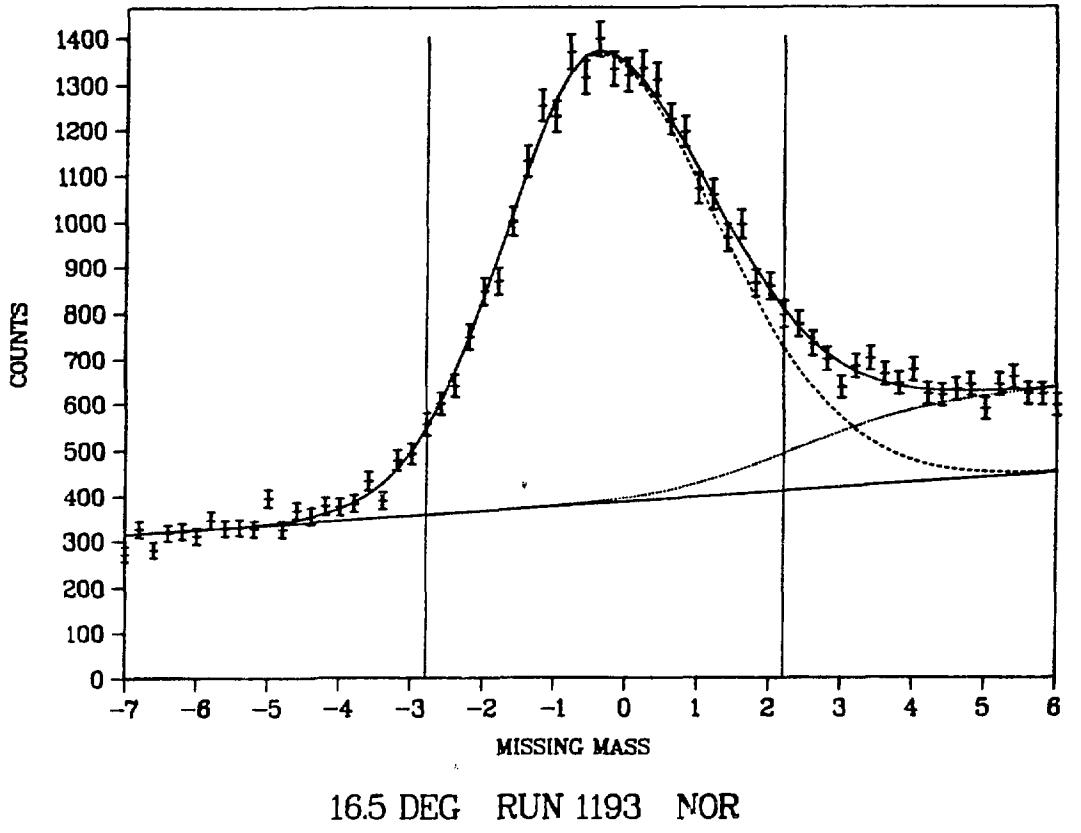

Figure VII-1

Typical fit at 16.5 degrees. The units on the horizontal axis are MeV and the gate is that used to select events for the FPP sums. The total fit and background are drawn with solid lines. The dashed curve is the background plus deuteron elastic peak and the dotted curve is the background plus deuteron breakup.

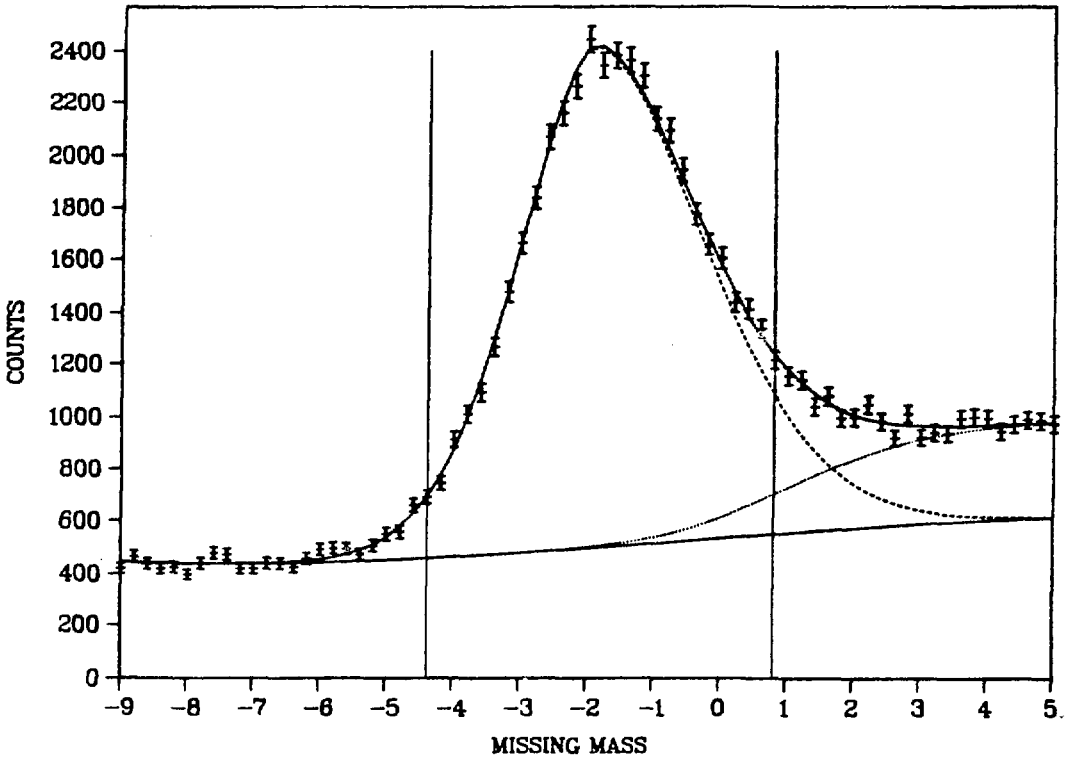

Figure VII-2

Typical fit at 14 degrees. The units on the horizontal axis are MeV and the gate is that used to select events for the FPP sums. The curves are the same as those on figure 1.

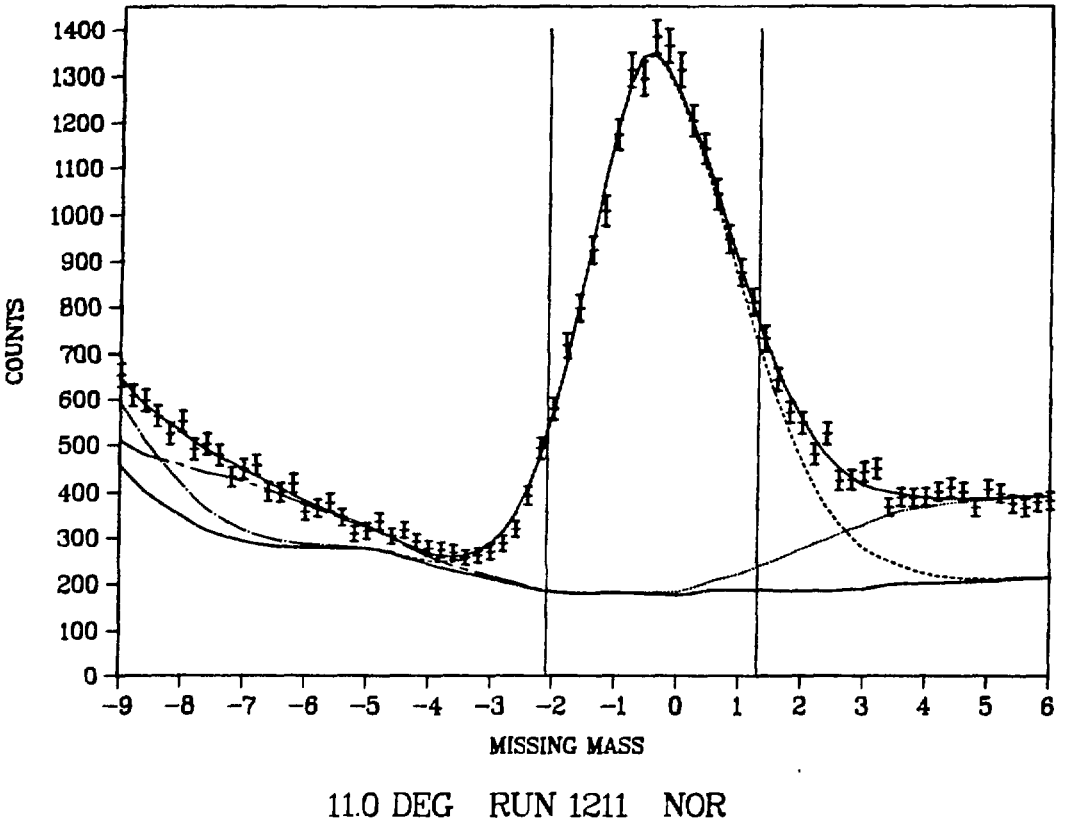

Figure VII-3

Typical fit at 11 degrees. The units on the horizontal axis are MeV and the gate is that used to select events for the FPP sums. The long-short dashed curve is the background plus ^{3}He and the dash-dot curve is the background plus ^{4}He. The remaining curves are the same as those as on figure 1.

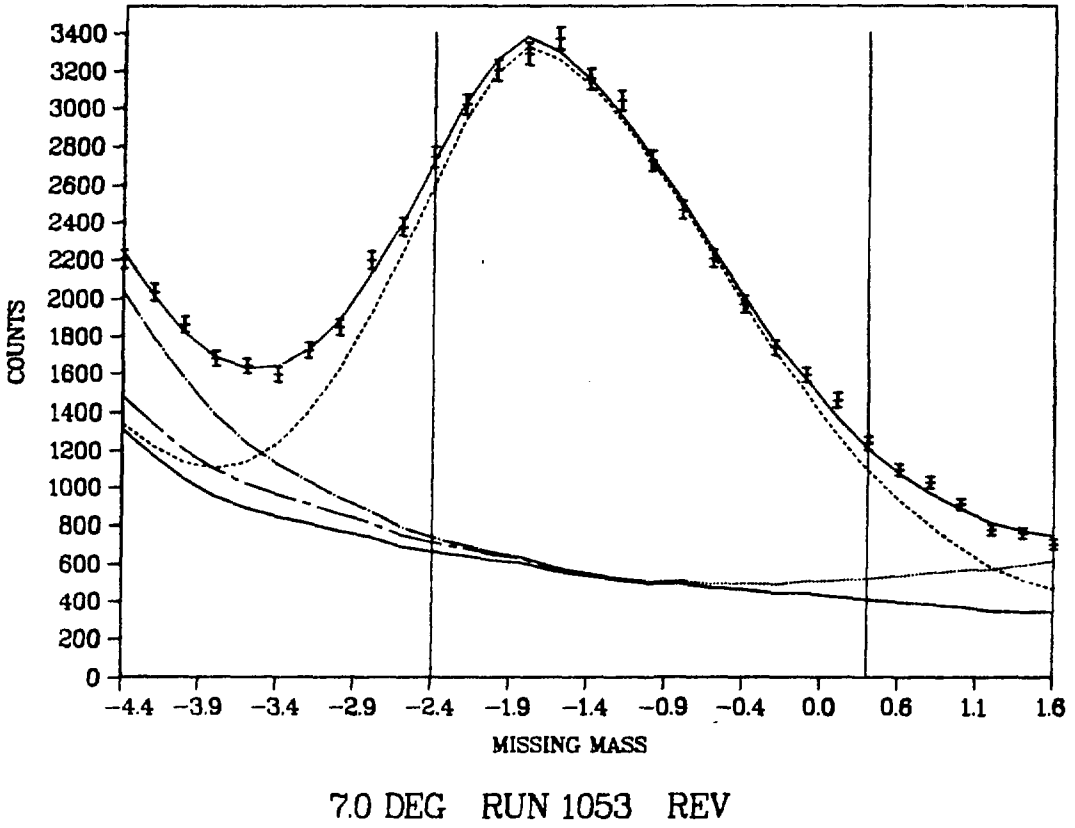

Figure VII-4

Typical fit at 7 degrees. The units on the horizontal axis are MeV and the gate was used to select events for the FPP sums. The curves are the same as those on figure 3.

VIII. Focal Plane Polarizations

The polarization at the focal plane was calculated by taking appropriate sums involving the polar, θ_c, and azimuthal, ϕ_c, scattering angles in the carbon blocks. The method we used is discussed in references 18 and 19. The latter paper deals specifically with the HRS focal plane polarimeter. As usual, a right handed coordinate system $(\hat{S}, \hat{N}, \hat{L})$ is used to describe the polarization with $\hat{L}$ along the direction of motion incident on the carbon. This coordinate system and the angles θ_c and ϕ_c are shown in figure III-6. The distribution of scattering angles depends on the transverse components of the polarization, p_S and p_N,

$$I(\theta_c,\phi_c) = I_0(\theta_c)\,[1 + A(\theta_c)\,p_N \cos\phi_c - A(\theta_c)\,p_S \sin\phi_c]\,G(\theta_c,\phi_c)\ .$$

Here $I_0(\theta_c)$ is the distribution for unpolarized events, $A(\theta_c)$ is the effective analyzing power for the carbon, and $G(\theta_c,\phi_c)$ is the acceptance.

We made use of the $\phi + \pi$ test in which the acceptance is required to satisfy $G(\theta_c,\phi_c) = G(\theta_c,\phi_c+\pi)$. This is called the weighted sums estimator in reference 18. The condition is enforced by discarding events which scatter at (θ_c, ϕ_c) when $(\theta_c, \phi_c + \pi)$ lies outside of the physical acceptance. With this acceptance function, a Fourier analysis of the angular distribution yields

$$\int I(\theta_c,\phi_c)\cos\phi_c\, d\phi_c = A(\theta_c)\, p_N \int I(\theta_c,\phi_c)\cos^2\phi_c\, d\phi_c - A(\theta_c)\, p_S \int I(\theta_c,\phi_c)\sin\phi_c\cos\phi_c\, d\phi_c$$

$$\int I(\theta_c,\phi_c)\sin\phi_c\, d\phi_c = A(\theta_c)\, p_N \int I(\theta_c,\phi_c)\sin\phi_c\cos\phi_c\, d\phi_c - A(\theta_c)\, p_S \int I(\theta_c,\phi_c)\sin^2\phi_c\, d\phi_c$$

where the integration is always taken over the full angular range from 0 to 2π.

For a given polar angle, θ_c, the integrals may be approximated by event sums to obtain

$$\Sigma\cos\phi_c = A(\theta_c)\, p_N\, \Sigma\cos^2\phi_c - A(\theta_c)\, p_S\, \Sigma\sin\phi_c\cos\phi_c$$

$$\Sigma\sin\phi_c = A(\theta_c)\, p_N\, \Sigma\sin\phi_c\cos\phi_c - A(\theta_c)\, p_S\, \Sigma\sin^2\phi_c\ .$$

These equations are now weighted by the analyzing power and the full range of polar angles is included in the event sums to obtain the matrix equation

$$\begin{pmatrix} \Sigma\, A\cos\phi_c \\ -\Sigma\, A\sin\phi_c \end{pmatrix} = \begin{pmatrix} \Sigma\, A^2\cos^2\phi_c & -\Sigma\, A^2\sin\phi_c\cos\phi_c \\ -\Sigma\, A^2\sin\phi_c\cos\phi_c & \Sigma\, A^2\sin^2\phi_c \end{pmatrix} \begin{pmatrix} p_N \\ p_S \end{pmatrix}\ .$$

The two components of polarization are obtained inverting the matrix and applying it to the left hand side. The inverse matrix is approximately the error matrix for p_N and p_S[18] and consequently the

diagonal elements of this matrix are the squares of their uncertainties.

The effective carbon analyzing power was obtained from the fit of McNaughton et al.[20] and was binned in one degree steps. The analyzing power used for angles between n - 0.5 and n + 0.5 degrees was the fit value at n degrees where n is an integer. We included only those events with polar scattering angles between 4.5 and 20.5 degrees. The effective analyzing power depends on the average energy of the proton at the center of the carbon which is different for different angular settings of the HRS. The analyzing powers used for this experiment are listed in table 1.

θ_c	θ_{HRS}			
	7	11	14	16.5
5	0.2223	0.2299	0.2359	0.2406
6	0.2454	0.2532	0.2598	0.2652
7	0.2549	0.2627	0.2694	0.2750
8	0.2543	0.2613	0.2675	0.2729
9	0.2484	0.2540	0.2592	0.2638
10	0.2413	0.2450	0.2488	0.2522
11	0.2351	0.2369	0.2389	0.2411
12	0.2305	0.2303	0.2307	0.2316
13	0.2272	0.2252	0.2242	0.2239
14	0.2248	0.2213	0.2190	0.2177
15	0.2229	0.2181	0.2147	0.2125
16	0.2209	0.2151	0.2109	0.2080
17	0.2186	0.2120	0.2071	0.2036
18	0.2157	0.2085	0.2031	0.1992
19	0.2120	0.2044	0.1985	0.1943
20	0.2074	0.1995	0.1934	0.1890

Table VIII-1

Effective carbon analyzing powers used to calculate focal plane polarizations.

IX. Extraction of Analyzing Powers

The expression (II-3) which connects the measured asymmetries and the analyzing powers can be rewritten as

$$(1 + \frac{1}{2}A_{OLL}P_T)\ \varepsilon = A_{NO}P_N + \frac{3}{2}A_{SL}P_S + \frac{3}{2}A_{LL}P_L P + \frac{1}{2}A_{NLL}P_N P_T \ . \qquad (1)$$

This expression assumes invariance under parity. The four analyzing powers which appear on the right hand side of equation 1 have been extracted at each angle using the least squares technique outlined in appendix E. The asymmetry, the magnitude and two LCPO directions of the beam polarization, and the magnitude of the target polarization were assumed to be independent measurements and their uncertainties were combined in quadrature to obtain the weight factors for the fit. The uncorrelated analyzing power A_{OLL} was calculated from the measurements done by Haji-Saeid et al.[11] This term amounts only to at most a one percent correction to the left hand side. Systematic uncertainties are negligible for all analyzing powers except A_{NO} for which an uncertainty of 2% should be added (see appendix B).

The data set at each angle consisted of nine to eleven measurements including each beam and target orientation and at least two unpolarized target runs. The chi squares for the fits ranged from 2.5 to 8.2. The values and uncertainties obtained for these four analyzing powers are given in table 1 and in figures 1-3. The values for A_{NO} have been adjusted as described in appendix B to account for finite acceptance of the HRS. Our values for the uncorrelated

analyzing power A_{NO} show good agreement with the results of Irom et al.[8] at the smaller angles and with those of Winkelman et al.[9] at larger angles. Both of these data sets were also taken at LAMPF but did not make use of the HRS.

It is useful to including parity violating terms because they provide checks. Our data sets are sufficiently overcomplete that we can add the two uncorrelated analyzing powers A_{SO} and A_{LO} as well as the vector correlated analyzing power A_{NL}. Tensor correlated, parity violating terms are not included because we do not have enough measurements to determine all of them and the small tensor polarization ensures little sensitivity to them. The relationship between the asymmetry and this expanded set of analyzing powers is

$$(1 + \frac{1}{2}A_{OLL}P_T)\,\varepsilon = A_{NO}P_N + A_{SO}P_S + A_{LO}P_L + \frac{3}{2}A_{SL}P_S + \frac{3}{2}A_{LL}P_LP + \frac{3}{2}A_{NL}P_NP + \frac{1}{2}A_{NLL}P_NP_T \cdot \qquad (2)$$

All seven of the analyzing powers which appear on the right hand side were extracted by doing a least squares fit based on this equation. The values obtained for the parity forbidden analyzing powers are also presented in table 1 and in figures 1 and 2. These are generally consistent with zero. The values obtained for the parity allowed observables were not significantly different than those obtained with the first fit.

	θ_{HRS}			
	7	11	14	16.5
A^*_{SO}	-0.001 (8)	0.000 (9)	-0.010 (10)	-0.006 (10)
A^*_{LO}	0.001 (9)	0.001 (8)	-0.001 (9)	0.007 (9)
A_{NO}	0.351 (9)	0.437 (10)	0.411 (11)	0.380 (11)
A^*_{NL}	-0.008 (23)	0.042 (21)	0.009 (22)	0.004 (23)
A_{SL}	-0.014 (19)	0.029 (20)	-0.014 (22)	-0.037 (24)
A_{LL}	0.139 (19)	0.078 (19)	0.027 (18)	-0.007 (21)
A_{NLL}	0.17 (31)	0.17 (32)	0.60 (33)	0.95 (36)

Table IX-1

Measured analyzing powers. Quantity in parentheses is the uncertainty in the last digit(s). The analyzing powers marked with asterisks are parity forbidden.

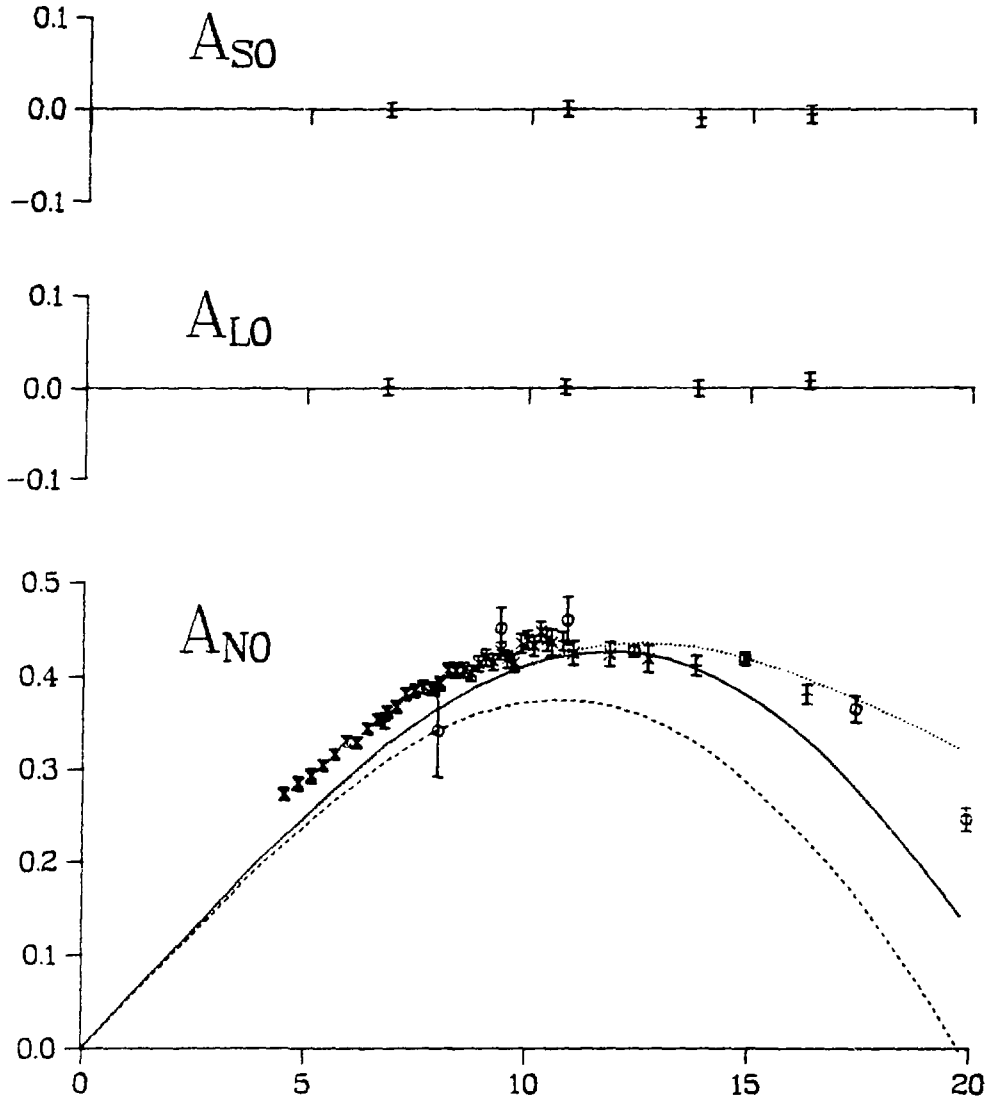

Figure IX-1

Uncorrelated analyzing powers. The top two are parity forbidden. The horizontal axis is the laboratory scattering angle in degrees. For A_{NO}, the crosses are taken from Irom et al.,[8] the circles from Winkleman et al.,[9] and our points are marked with the same symbols and appear at the same angles as for A_{SO} and A_{LO}. The curves are discussed in chapter XI.

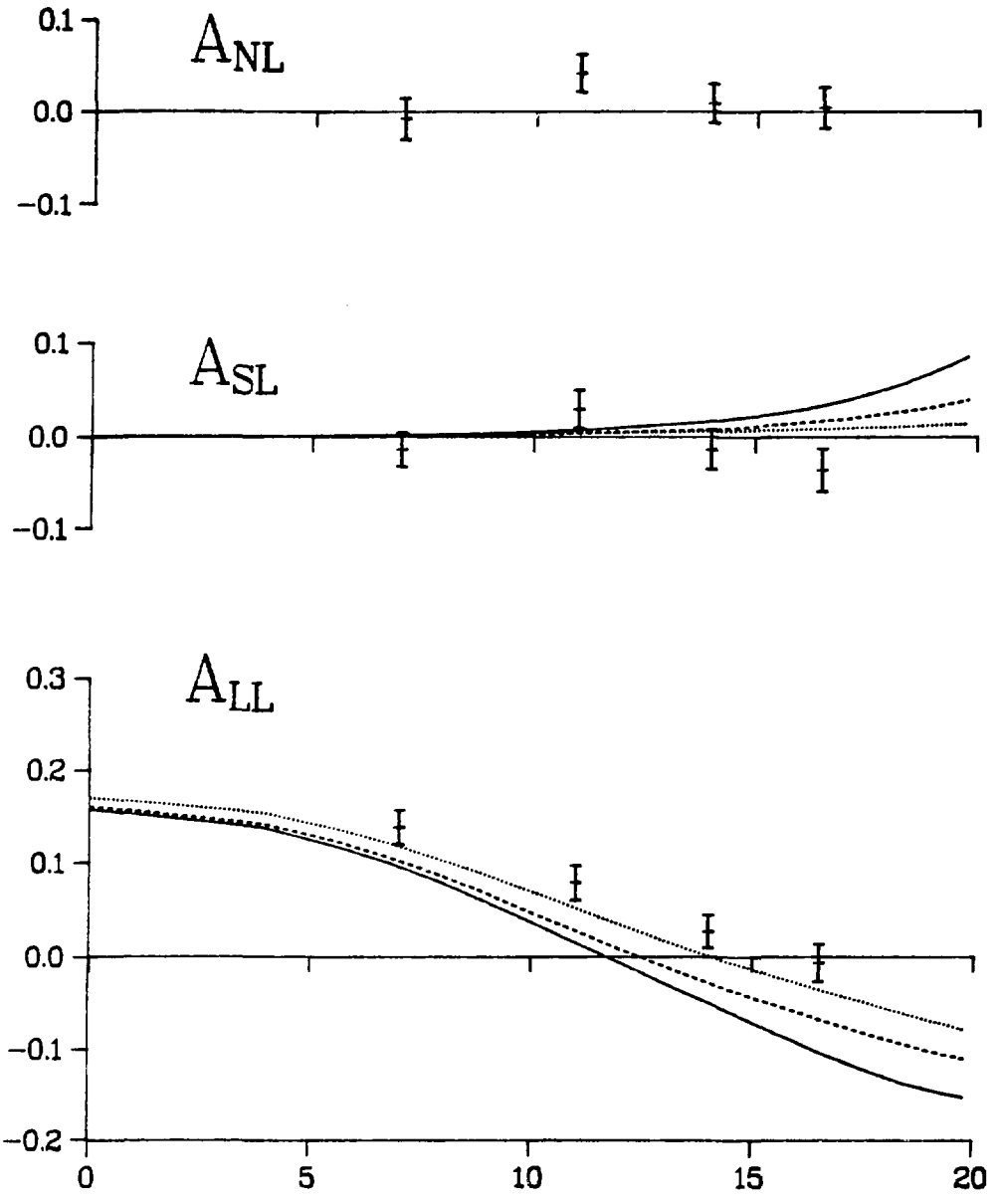

Figure IX-2

Vector correlated analyzing powers. The top one is parity forbidden. The horizontal axis is the laboratory scattering angle in degrees. The curves are discussed in chapter XI.

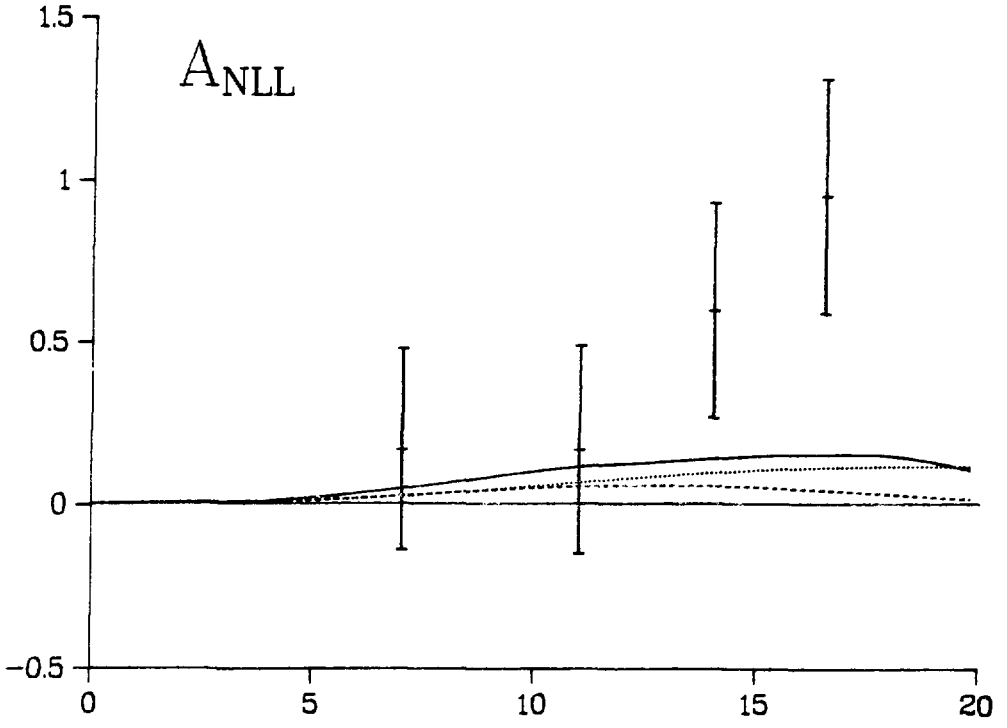

Figure IX-3

Tensor correlated analyzing power. The horizontal axis is the laboratory scattering angle in degrees. The curves are discussed in chapter XI.

X. Extraction of Spin Transfer Coefficients

The polarization of the scattered proton may be expressed as a linear function of the six spin transfer coefficients of interest and six linear combinations of other spin transfer coefficients which do not involve the vector polarization of the deuteron (equation II-4). It is convenient to define twelve parameters K_{ia} (i = S,N,L; a = 0,S,N,L) to treat both sets collectively:

$$K_{OS} = C_{OL,S}$$
$$K_{ON} = C_{OO,N} + \frac{1}{2} C_{OLL,N} P_T + r D_{ON}$$
$$K_{OL} = C_{OL,L}$$
$$K_{SS} = C_{SO,S} + \frac{1}{2} C_{SLL,S} P_T + r D_{SS}$$
$$K_{NS} = C_{NL,S}$$
$$K_{LS} = C_{LO,S} + \frac{1}{2} C_{LLL,S} P_T + r D_{LS}$$
$$K_{SN} = C_{SL,N}$$
$$K_{NN} = C_{NO,N} + \frac{1}{2} C_{NLL,N} P_T + r D_{NN}$$
$$K_{LN} = C_{LL,N}$$
$$K_{SL} = C_{SO,L} + \frac{1}{2} C_{SLL,L} P_T + r D_{SL}$$
$$K_{NL} = C_{NL,L}$$
$$K_{LL} = C_{LO,L} + \frac{1}{2} C_{LLL,L} P_T + r D_{LL} .$$

These parameters will be determined with a least squares fit and must be assumed to be constant. This is obviously true for the vector parameters (OS,OL,SN,NS,NL,LN) because our angular and missing mass acceptances did not change significantly between runs. The combination parameters (ON,SS,SL,NN,LS,LL) are not constant because

the tensor polarization, P_T, the unpolarized background to deuteron ratio, r, and the background spin transfer coefficients, D_{ai}, could vary slightly from run to run. However, because all these effects are estimated to change the combination parameters by less than 0.01, we have treated them as constant.

The polarization of the scattered proton measured at the focal plane is related to that at the target by a rotation U which accounts for spin precession in the target holding field and the fields of the spectrometer magnets: $p_j^{fp} = \Sigma\, U_{ji}\, p'_i$. The linear relationships between the focal plane polarizations measured for normal and reverse beam and the parameters K_{ai} are

$$p_j^{fp}(\text{nor}) = \Sigma\, x_{j,ai}\, K_{ai}$$
$$p_j^{fp}(\text{rev}) = \Sigma\, x'_{j,ai}\, K_{ai} \qquad (1)$$

$$x_{j,SO} = \frac{3}{2} R\, U_{jS}\, P \qquad x'_{j,SO} = \frac{3}{2} R'\, U_{jS}\, P$$
$$x_{j,NO} = R\, U_{jN} \qquad x'_{j,NO} = R'\, U_{jN}$$
$$x_{j,LO} = \frac{3}{2} R\, U_{jL}\, P \qquad x'_{j,LO} = \frac{3}{2} R'\, U_{jL}\, P$$
$$x_{j,SS} = R\, U_{jS}\, P_S \qquad x'_{j,SS} = -R'\, U_{Sj}\, P_S$$
$$x_{j,NS} = \frac{3}{2} R\, U_{jN}\, P\, P_S \qquad x'_{j,NS} = -\frac{3}{2} R'\, U_{jN}\, P\, P_S$$
$$x_{j,LS} = R\, U_{jL}\, P_S \qquad x'_{j,LS} = -R'\, U_{jL}\, P_S$$
$$x_{j,SN} = \frac{3}{2} R\, U_{jS}\, P\, P_N \qquad x'_{j,SN} = -\frac{3}{2} R'\, U_{jS}\, P\, P_N$$
$$x_{j,NN} = R\, U_{jN}\, P_N \qquad x'_{j,NN} = -R'\, U_{jN}\, P_N$$
$$x_{j,LN} = \frac{3}{2} R\, U_{jL}\, P\, P_N \qquad x'_{j,LN} = -\frac{3}{2} R'\, U_{jL}\, P\, P_N$$
$$x_{j,SL} = R\, U_{jS}\, P_L \qquad x'_{j,SL} = -R'\, U_{jS}\, P_L$$
$$x_{j,NL} = \frac{3}{2} R\, U_{jN}\, P\, P_L \qquad x'_{j,NL} = -\frac{3}{2} R'\, U_{jN}\, P\, P_L$$
$$x_{j,LL} = R\, U_{jL}\, P_L \qquad x'_{j,LL} = -R'\, U_{jL}\, P_L \,.$$

Here $R = Y_0(d)/Y(tot)$ is the yield ratio for the normal beam state and R' is the same ratio for reverse beam.

Thus, to determine the parameters K_{ai}, it is necessary to know the yield ratios R and R', and the rotation matrix U in addition to the beam, target, and focal plane polarizations. The measurement of each of the polarizations has already been discussed.

The yield ratio can be expressed as a product of ratios,

$$R = \frac{Y_0(d)}{Y(tot)} = \frac{Y_0(d)}{Y(d)} \frac{Y(d)}{Y(tot)}$$

The first ratio can be obtained immediately from the analyzing powers and incoming polarizations (equation II-1). The second ratio was obtained by fitting the spectra in a manner similar to that used for the analyzing powers. The peaks in the fitted spectra were then integrated over the same region over which the focal plane polarimeter sums were taken. The uncertainty in the ratio R was taken to be 2% at 14 and 16.5 degrees, 3% at 11 degrees, and 5% at 7 degrees.

The two rotations which make up the overall spin rotation U were evaluated separately. The spin precession in the field of the target magnet was calculated using the field map as described in appendix C. The rotation at 11 degrees with the ordering (S, N, L) was

$$U_{target} = \begin{bmatrix} 0.970 & 0.243 & -0.006 \\ -0.243 & 0.970 & -0.028 \\ -0.001 & 0.028 & 1.000 \end{bmatrix} .$$

The components of the rotations at the other angles were all within 0.02 of these. The precession of the proton spins in the spectrometer magnets was assumed to take place only about the $\hat{S}$ direction and the precession angle was calculated on an event by event basis during the replay of the data. The average angle for each series of runs was used to construct the rotation matrix. This angle varied from 485 to 496 degrees.

The $\hat{S}$ and $\hat{N}$ components of the focal plane polarization were measured for both normal and reverse beam providing four measurements for each orientation of the beam and target polarizations. These four polarization components were not fit directly. Instead, differences and sums of normal and reverse polarizations were fit so that an extra uncertainty in could be added to the sums. This extra uncertainty allows for fluctuations in the false polarization due to instrumental asymmetries. The least squares fit described in appendix E was done using the following four equations for each orientation of the beam and target polarizations:

$$\begin{aligned}
p_S^{fp}(nor) - p_S^{fp}(rev) &= \Sigma\, (x_{S,ia} - x'_{S,ia})\, K_{ia} \\
p_S^{fp}(nor) + p_S^{fp}(rev) &= \Sigma\, (x_{S,ia} + x'_{S,ia})\, K_{ia} + 2\, p_S^0 \\
p_N^{fp}(nor) - p_N^{fp}(rev) &= \Sigma\, (x_{N,ia} - x'_{N,ia})\, K_{ia} \\
p_N^{fp}(nor) + p_N^{fp}(rev) &= \Sigma\, (x_{N,ia} + x'_{N,ia})\, K_{ia}
\end{aligned} \qquad (2)$$

The extra term in the second equation allows for a false polarization in the $\hat{S}$ direction. A false polarization in the $\hat{N}$ direction is absorbed by the parameter K_{ON}.

The uncertainties in the beam and target polarizations and in the yield ratio as well as those in the focal plane polarization were included with all four equations. The extra uncertainty added to the sums (the second and fourth of equations 2) was determined by calculating separate chi-squares for the sums and the differences (the first and third equations). The final value for this extra uncertainty was chosen to be that which gave roughly equal equal chi-squares for the sums and differences. The same value of 0.05 was used at all angles. This uncertainty, the uncertainty in the focal plane polarization and to a lesser extent that in the beam polarization dominated. Final results for the six spin transfer coefficients of interest are presented in table 1 and figures 1 and 2.

Our measurements included seven or eight sets of focal plane polarizations at each angle because the data for one or two of the orientations of the beam and target polarizations were taken in two parts. The chi squares for the fits ranged from 8 to 24 corresponding to reduced chi squares in the range 0.5 to 1.3. The chi squares for the sums varied from 6 to 16 and those for the differences from 0.4 to 11. The final value for the extra uncertainty in the sums is somewhat larger than the observed fluctuation in the S-component of false

	θ_{HRS}			
	7	11	14	16.5
$C_{OL,S}$	-0.035 (42)	0.007 (37)	-0.051 (42)	-0.082 (53)
$C_{OL,L}$	0.120 (58)	0.055 (49)	0.001 (52)	0.077 (63)
$C_{SL,N}$	-0.014 (104)	0.040 (96)	-0.009 (110)	0.006 (158)
$C_{NL,S}$	-0.044 (72)	-0.044 (64)	0.000 (66)	-0.102 (88)
$C_{NL,L}$	-0.076 (132)	-0.061 (97)	0.088 (94)	0.205 (114)
$C_{LL,N}$	-0.102 (129)	-0.077 (104)	-0.251 (116)	-0.185 (163)

Table IX-1

Measured spin transfer coefficients. Quantity in parentheses is the uncertainty in the last digits.

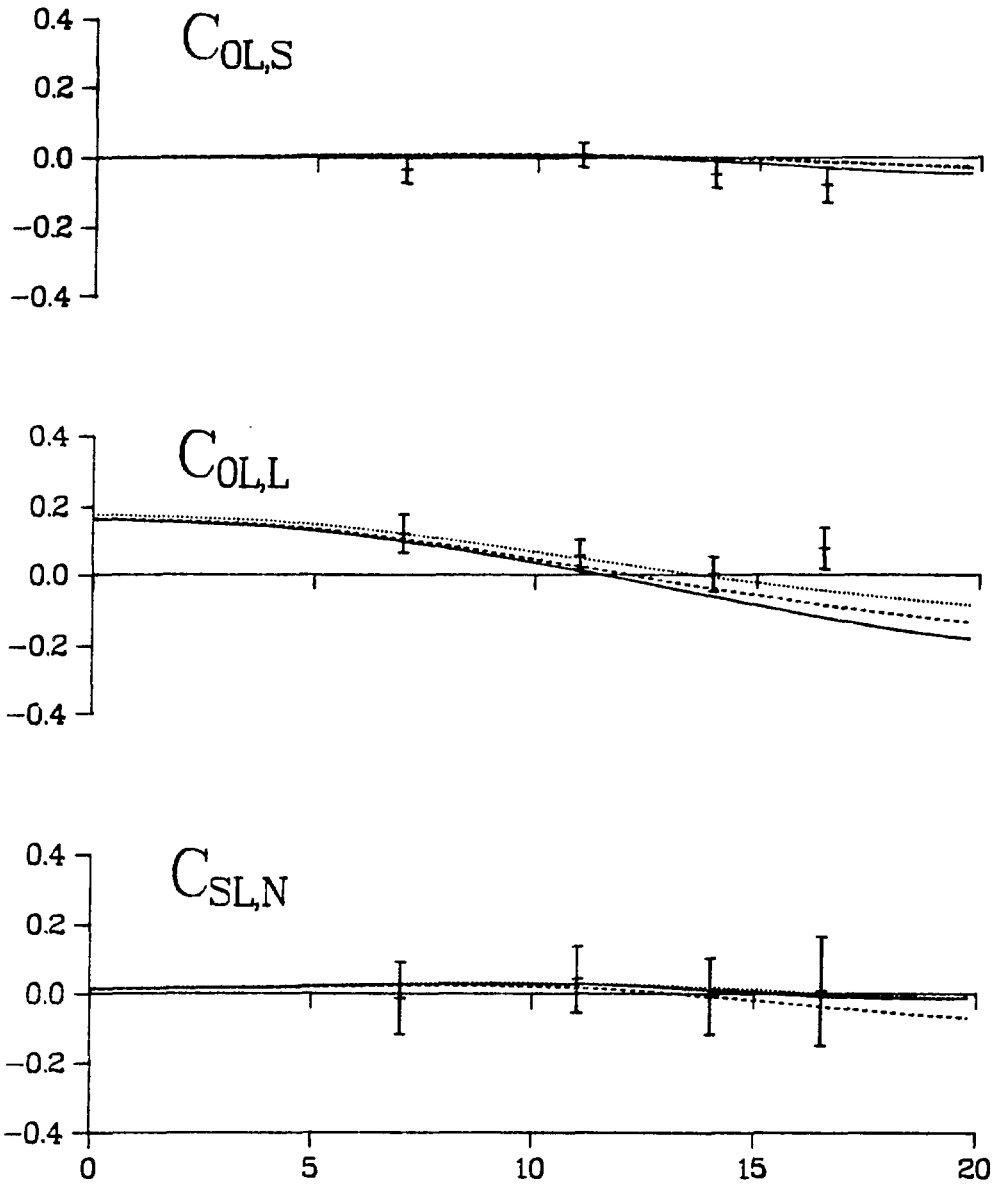

Figure X-1

Spin transfer coefficients $C_{OL,S}$, $C_{OL,L}$, and $C_{SL,N}$. The horizontal axis is the scattering angle in degrees. The curves are discussed in chapter XI.

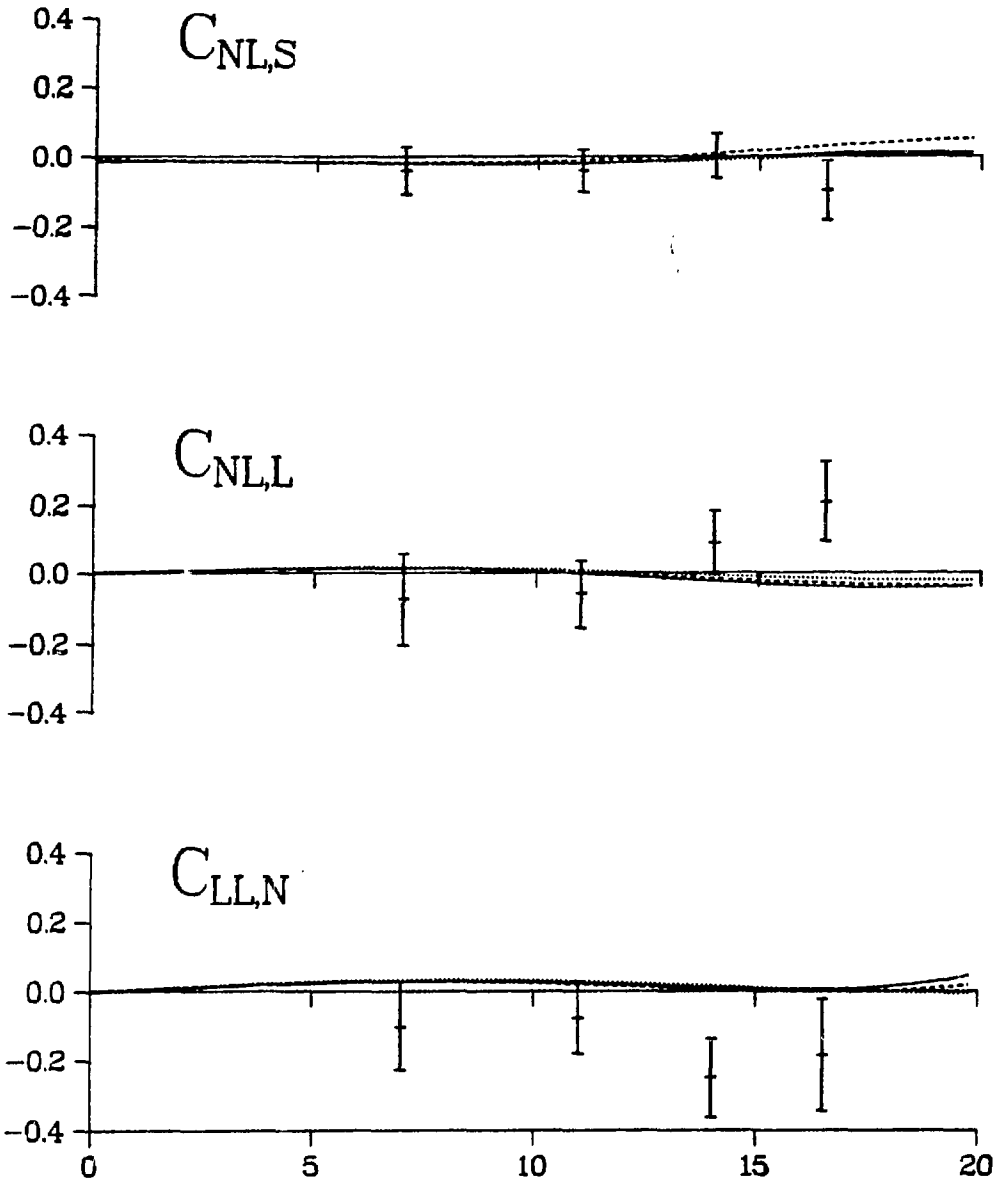

Figure X-2

Spin transfer coefficients $C_{NL,S}$, $C_{NL,L}$, and $C_{LL,N}$. The horizontal axis is the scattering angle in degrees. The curves are discussed in chapter XI.

polarization, p_S^0. The four different angles gave values of 0.07, 0.04, 0.02, and 0.01 for this parameter.

XI. Conclusions

The observables measured in this experiment do not, by themselves, place any tight constraints on the theoretical description of proton-deuteron elastic scattering because of its complex spin structure. Instead, this experiment is one of a series whose results will be combined to completely determine the proton-deuteron elastic scattering matrix at the energy and over the range of momentum transfer discussed here. Other experiments in the series include the first part of LAMPF experiment 685 performed in the summer of 1983 with an N-type target and the unpolarized target experiments described in references 8-11. The existing data, when completely analyzed, will probably be barely adequate for this task and an attempt to reconstruct the scattering matrix will reveal which, if any, experiments are required to complete the job. We are also performing a series of experiments covering a region of higher momentum transfer which will be used to extend these results.

It is, of course, possible to use a scattering matrix taken from a theoretical calculation to make predictions for any observable. We present the results for a few such calculations, compare with our measured values, and make a few preliminary comments.

The calculations discussed here are extensions of the multiple scattering theory developed in reference 22. The scattering of a proton from a deuteron is described as the sum of single and double scattering terms in which the incident proton scatters from one or

both of the nucleons in the deuteron. The components of the calculation are a deuteron wave function, separate scattering matrices to describe the proton-proton and proton-neutron interactions, and, for double scattering, a propagator for the intermediate state nucleon. The wave function used in the calculations discussed here is that of reference 23 and the propagator is that which follows from the free Dirac equation. A major development since the publication of reference 22 is the introduction of relativistic nucleon-nucleon scattering matrices which are expressed in terms of Dirac operators instead of Pauli operators.

Assuming invariance under parity and time reversal, the on-shell part of either nucleon-nucleon matrix may be written as the sum of five independent spin operators (either Pauli or Dirac) each multiplied by a complex function of an energy variable and a momentum transfer variable. These functions are evaluated by requiring that the matrices be in agreement with the nucleon-nucleon phase shift analysis of reference 24. The off-shell parts of the matrices are determined by using the on-shell values and ignoring possible dependences on off-shell parameters. There is some ambiguity present in the choice of energy (E_{cm}, E_{lab}, s, ...) and momentum transfer (θ_{cm}, θ_{lab}, t, ...) variables and their definitions off-shell. However, much more serious ambiguities are present in the relativistic matrices[25] since there are many more than five invariant (under parity and time reversal) Dirac operators which are independent off-shell. The off-shell behavior of these scattering matrices depends on the representation (i.e., on which five independent operators are used to

construct each matrix) even though all representations are required to have the same on-shell behavior. The motivation for introducing the more complicated relativistic form is the improvement often obtained in the description of other proton-nucleus scattering processes (e.g., references 1-4).

Here we present predictions based on two different representations of the nucleon-nucleon scattering matrices. The first is

$$F_{NN} = A + B\gamma_\mu\gamma^\mu + C\sigma_{\mu\nu}\sigma^{\mu\nu} + D(\gamma_5\gamma_\mu)(\gamma_5\gamma^\mu) + E\gamma_5\gamma_5$$

and the second is obtained by replacing the last term with $E(q^\mu\gamma_\mu\gamma_5)(q^\nu\gamma_\nu\gamma_5)$ where q^μ is the four momentum transfer. The notation used for the Dirac operators γ_μ, γ_5, and $\sigma_{\mu\nu}$ is that of Bjorken and Drell.[26] In each term, one Dirac operator acts in the spin space of the incident proton and the other in that of the target proton or neutron. The coefficients A, B, C, D, and E are functions of energy and momentum transfer as discussed above. The predictions are presented as curves on figures 1-3 of chapter IX and figures 1 and 2 of chapter X. The first curves (dotted) were calculated using only the single scattering term and so are the same for the nonrelativistic calculation or a relativistic calculation based on any representation of the nucleon-nucleon scattering matrices. The other two predictions include both single and double scattering terms and make use of relativistic representations of the nucleon-nucleon amplitudes. The

first of these (dashed) uses the representation in the equation above and the second (solid) uses the modified version.

Most of the observables we measured were found to have values near zero in agreement with any of these theoretical calculations. Two exceptions are the analyzing powers A_{N0} and A_{LL} for which there is some discrepancy between the measured and predicted values. Although the inclusion of double scattering does not improve these predictions, it does have some effect indicating that double scattering can make significant contributions even in this small momentum transfer region. Another possible explanation for the discrepancy between prediction and experiment is that the neutron-proton phase shifts are still not completely determined in our energy range.[24] However, neutron-proton scattering is a very active region experimentally and these should be better determined in the near future. Once the on-shell nucleon-nucleon scattering matrices have been well determined, this and other proton-deuteron elastic experiments may provide important information about the off-shell character of the nucleon-nucleon interaction.

References

1. J. Shepard, J. A. McNeil, and S. J. Wallace, Phys. Rev. Lett. 50 (1983) 1439

2. J. A. McNeil, J. Shepard, and S. J. Wallace, Phys. Rev. Lett. 50 (1983) 1443

3. B. C. Clark et al., Phys. Rev. Lett. 50 (1983) 1644

4. B. C. Clark et al., Phys. Rev. C28 (1983) 1421

5. D. L. Adams and M. Bleszynski Phys. Lett. 150B (1985) 405

6. M. Bleszynski, AIP Proceedings of the Second International Conference on Intersections Between Particle and Nuclear Physics, May 1986, to be published

7. L. Wolfenstein, Phys. Rev. 96 (1954) 1654

8. F. Irom et al., Phys. Rev. C28, (1983) 2380

9. E. Winkelman et al., Phys. Rev. C21, (1980) 2535

10. G. S. Weston, Los Alamos National Laboratory report LA-10174-T (1984)

11. M. Haji-Saeid et al., Phys. Lett., 106B (1981) 42

12. G. G. Ohlsen, Los Alamos National Laboratory report LA-4451 (1970)

13. M. W. McNaughton, Los Alamos National Laboratory report LA-8307 (1980)

14. M. W. McNaughton, Phys. Rev. C24, (1981) 1778

15. M. Borghini and K. Scheffler, Nucl. Instr. Meth. 95 (1971) 93

16. F. Sperisen, "Progress at LAMPF," Los Alamos National Laboratory Report LA-10738-PR (1986) and to be submitted to Nucl. Instr. Meth.

17. A. Azizi, Los Alamos National Laboratory Report LA-10493-T (1985)

18. D. Besset et al., Nucl. Instr. Meth. 166, 515 (1979)

19. J. B. McClelland et al., Los Alamos National Laboratory Report LA-UR-84-1671 (1985) and submitted to Nucl. Instr. Meth.

20. M. W. McNaughton, Nucl. Instr. Meth. A241, (1985) 435

21. W. Cornelius, Los Alamos National Laboratory Report LA-9130-MS (1981)

22. G. Alberi, M. Bleszynski, and T. Jaroszewicz, Ann. Phys. 142 (1982) 299

23. R. V. Reid, Ann. Phys. 50 (1978) 411.

24. R. A. Arndt et al., Phys. Rev. D28, (1983) 97

25. D. L. Adams and M. Bleszynski, Phys. Lett. 136B (1984) 10

26. J. Bjorken and S. Drell, Relativistic Quantum Mechanics, (McGraw-Hill, 1964)

27. J. D. Jackson, Classical Electrodynamics, 2nd ed., (Wiley, 1975) equation 11.170

A. Background Contributions to the Outgoing Polarization

The subset of events used to calculate the polarization of the scattered proton includes events from other reactions in addition to those from proton-deuteron elastic scattering. Here we first demonstrate that the unpolarized background contributions can be described collectively with a single set of constant spin transfer coefficients. We then discuss our neglect of contributions from inelastic proton-deuteron scattering. Finally, the missing mass gates used in the event selection are described.

Most of the background involves scattering from unpolarized nuclei in the target. Assume each reaction s contributes Y(s) events with polarization components $p_i'(s)$ (i = S,N,L) to this background. The net polarization of the background is just the weighted average

$$p_i' = \Sigma \frac{Y(s)}{Y(bg)} p_i'(s)$$

where $Y(bg) = \Sigma\, Y(s)$. The outgoing polarization for each reaction depends on the beam polarization, p_a (a = 0,S,N,L; $p_0 = 1$), and the spin transfer coefficients, $D_{ai}(s)$, which describe the reaction:

$$p_i'(s) = \frac{Y_0(s)}{Y(s)} \Sigma\, D_{ai}(s)\, p_a \ .$$

Here Y_0 is the number of events that would have been obtained with an unpolarized beam. The net polarization is

$$p_i'(bg) = \Sigma \frac{Y_0(s)}{Y(bg)} \Sigma D_{ai}(s)\, p_a \ .$$

We would like to collectively treat all contributions from unpolarized background materials. This is accomplished by introducing effective spin transfer coefficients, D_{ai}, which satisfy

$$p_i'(bg) = \frac{Y_0(bg)}{Y(bg)} \Sigma D_{ai}\, p_a$$

where $Y_0(bg)$ is the background yield with an unpolarized beam. Comparing the previous two equations, we find

$$D_{ai} = \Sigma \frac{Y_0(s)}{Y_0(bg)} D_{ai}(s) \ .$$

These effective coefficients are useful only if they remain fairly constant which will be true as long as the ratios $Y_0(s)/Y_0(bg)$ do not change significantly from run to run. Because these ratios only involve unpolarized yields, the effective coefficients do not depend explicitly on the beam or target polarization. It is only necessary to ensure that the event selection be the same for all runs. This was accomplished on line by using the same target for all runs and regularly verifying that the position of the beam on the target had not changed. Off line, the missing mass gate used to select events for the outgoing polarization calculation was set at the same position for all runs at each angle. Also, the gate at seven degrees was set

to minimize contributions from the helium elastic peaks because the helium level varied between runs.

A few breakup events in which protons scatter inelastically from the polarized deuterons are also included in the calculation of the scattered proton polarization. Using the same arguments as for the unpolarized background, we find that the deuteron observables that we measure are actually a mixture of elastic and inelastic observables. Denote the elastic and inelastic yields by Y(el) and Y(in), respectively and let Y(d) be the sum of these. Equations 2 of chapter II remain valid with $Y_0 = Y_0(el)$, $Y = Y(d)$, and

$$C_{a\alpha,i} = C_{a\alpha,i}(el) + \frac{Y_0(in)}{Y_0(el)} C_{a\alpha,i}(in) .$$

The gates on the missing mass spectra were chosen to minimize the contribution of these inelastic processes so that the yield ratio in the second term was always less than 0.02. For this reason, the contribution of this inelastic process has been ignored.

One of the tests used for selecting events to be used in the calculation of the scattered proton polarization was a gate on the missing mass spectrum. The right hand limit (greater missing mass) was chosen to keep the contribution from deuteron breakup below the level discussed above. At seven degrees, the left hand side was set to minimize contributions from the helium elastic peaks which increase rapidly with decreasing missing mass. At the other angles, the left hand limit was chosen to minimize the statistical errors in the

calculation of the observables. At each angle, the same gate was used for all spectra and the value used for the incident energy was adjusted so that the proton-deuteron elastic peak appeared at the same position for all runs. Typical spectra and the gates used are shown in figures 1-4 of chapter VII.

B. Systematic Corrections and Uncertainties

Here we discuss the importance of systematic uncertainties in the beam and target polarizations. We also discuss out of plane corrections due to the finite acceptance of the HRS. These systematic corrections and uncertainties are not important except in the relatively precise measurements of A_{NO} and the 180 degree A_{LL}. The statistical uncertainties for the values of A_{NO} are between 2 and 3% and the uncertainty for A_{LL} is 4% at 180 degrees. The statistical uncertainties for all other observables and angles are greater than 10%.

The systematic uncertainty in the magnitude of the beam polarization is that inherent in the quench measurement. Although this uncertainty can be as small as 0.5%,[12,13] it will be larger under normal running conditions unless special attention is devoted to the measurement. We estimate this uncertainty to be 2%. This systematic uncertainty contributes significantly only to the uncorrelated analyzing power A_{NO} and the 180 degree analyzing power A_{LL}.

The systematic uncertainty in the target polarization is estimated to be less than 0.01.[16] The observables involving the vector polarizations of the target depend primarily on the difference between the polarization in the parallel and anti-parallel configurations. These values were typically around 0.24 and -0.33. Assigning an uncertainty of 0.01 to each and combining these values in quadrature, we find this difference to have an uncertainty of 2.5%.

This is the systematic uncertainty due to the target polarization which we assign to the observables. It contributes significantly only to A_{LL} at 180 degrees.

The finite acceptance of the HRS implies in general that systematic corrections must be made to the S- and N-components of the beam and target polarizations to account for out of plane scattering. These corrections are required because the event averaged values for these components are not the same as the values corresponding to the center of the spectrometer acceptance. These corrections are discussed for the case of an unpolarized target in references 21 and 19. There are no corrections to the target polarization because it is purely L-type. The S-component of the beam polarization for the first beam type and the N-component for the last two types have been approximately overestimated by 1.4, 0.6, 0.3, and 0.2% at 7, 11, 14, and 16.5 degrees, respectively. These corrections are negligible except for the uncorrelated analyzing power A_{NO} for which the values have been increased by the above factors. The more complicated corrections to the scattered proton polarizations have been neglected because the statistical uncertainties for the corresponding observables are fairly large.

C. Trajectories and Spin Precession

The magnetic field used to maintain the target polarization changes the trajectories of the scattered protons and causes the spin of both incident and scattered protons to precess. Here we briefly discuss the equations which underlie the program used to calculate the trajectories and spin precession.

The trajectory is obtained from the usual equation of motion for a charged particle in a magnetic field:

$$\frac{d\underset{\sim}{p}}{dt} = \frac{q}{c}\,\underset{\sim}{v} \times \underset{\sim}{B} \ .$$

The momentum can be expressed in terms of the velocity, $\underset{\sim}{p} = \gamma m \underset{\sim}{v}$, where $\gamma = 1/\sqrt{1-(v/c)^2}$ is constant because a magnetic field can change only the direction and not the magnitude of the velocity. The change of velocity during an infinitesimal time Δt is

$$\Delta\underset{\sim}{v} = \frac{q}{\gamma m c}\,(\underset{\sim}{v} \times \underset{\sim}{B})\,\Delta t \ .$$

The computer code makes use of this expression and the change of position $\Delta\underset{\sim}{x} = \underset{\sim}{v}\,\Delta t$ to calculate the trajectory in small but finite increments Δt.

The calculation of the spin precession is more complicated. In the laboratory frame, the spin precession is given by[27]

$$\frac{d\underset{\sim}{s}}{dt} = \frac{q}{mc}\,\underset{\sim}{s} \times \left[\left(\frac{g}{2} - 1 + \frac{1}{\gamma}\right)\underset{\sim}{B} - \left(\frac{g}{2} - 1\right)\frac{\gamma}{\gamma+1}\frac{1}{c^2}\,(\underset{\sim}{v}\cdot\underset{\sim}{B})\,\underset{\sim}{v}\right]$$

where g is the gyromagnetic ratio. But we wish to use a frame of reference which is attached to the changing direction of the velocity. We define an orthonormal coordinate system ($\hat{S}$, $\hat{N}$, $\hat{L}$) with $\hat{L}$ along the direction of motion and $\hat{S}$ in the horizontal plane:

$$\hat{L} = \frac{\underset{\sim}{v}}{v}$$

$$\hat{S} = \frac{\hat{y} \times \hat{L}}{\sin\theta}$$

$$\hat{N} = \hat{L} \times \hat{S}\ .$$

Here $\hat{y}$ is a unit vector in the vertical direction and θ is the angle between $\hat{y}$ and $\hat{L}$.

To calculate the spin precession in this non-inertial frame of reference, we must include the time rate of change of the coordinate system. It is convenient to express the magnetic field strength in this coordinate system, $B_i = \underset{\sim}{B}\cdot\hat{i}$ (i = S,N,L). The necessary rates are

$$\frac{d\hat{L}}{dt} = \frac{1}{v}\frac{d\underset{\sim}{v}}{dt}$$

$$= \frac{q}{\gamma mc}\,(-B_N\,\hat{S} + B_S\,\hat{N})$$

$$\frac{d\hat{S}}{dt} = \frac{\sin\theta\ \hat{y} \times (d\hat{L}/dt) - (\hat{y} \times \hat{L})\ (\cos\theta\ d\theta/dt)}{\sin^2\theta}$$

$$= \frac{q}{\gamma mc}\,(-\cot\theta\ B_N\,\hat{N} + B_N\,\hat{L})$$

$$\frac{d\hat{N}}{dt} = \frac{d\hat{L}}{dt} \times \hat{S} + \hat{L} \times \frac{d\hat{S}}{dt}$$

$$= \frac{q}{\gamma mc} (\cot\theta \, B_N \, \hat{S} - B_S \, \hat{L}) \, .$$

The time rate of change of each component of the spin is given by

$$\frac{ds_i}{dt} = \frac{d\underset{\sim}{s}}{dt} \cdot \hat{i} + \underset{\sim}{s} \cdot \frac{d\hat{i}}{dt} \qquad (i = S,N,L) \, .$$

The change of spin in the time Δt is

$$\Delta s_L = \frac{q}{mc} \left(\frac{g}{2} - 1\right) (B_N \, s_S - B_S \, s_N) \, \Delta t$$

$$\Delta s_S = \frac{q}{\gamma mc} \left\{ \left[\frac{g}{2} B_L - \cot\theta \, B_N\right] s_N - \left[\gamma \left(\frac{g}{2} - 1\right) B_N\right] s_L \right\} \Delta t$$

$$\Delta s_N = \frac{q}{\gamma mc} \left\{ \left[-\frac{g}{2} B_L + \cot\theta \, B_N\right] s_S + \left[\gamma\left(\frac{g}{2} - 1\right) B_S\right] s_L \right\} \Delta t \, .$$

The total spin precession is calculated by adding these contributions along the length of the trajectory.

D. Backward Scattering

Runs were regularly taken to measure the asymmetry in backward proton-deuteron elastic scattering. These runs determine the analyzing power A_{LL} at a scattering angle of 180 degrees and provide a rough check of the DMR measurement of the target polarization. For these runs, the HRS was moved to zero degrees and the fields of the spectrometer magnets were set to detect the recoil deuterons. The scattered protons were not detected. The carbon blocks were removed and the usual trigger (without SX) was used. Most of the data were taken with a beam intensity of 2×10^7 protons/sec which provided about 10 events/second.

Extraction of Asymmetries

As at the other angles, each of the backward scattered events was subjected to a series of tests and only those passing all tests were included in the missing mass histograms. These tests included the front chamber and PID tests described in chapter VI and one additional test, THTPHI. The limits for the PID tests were chosen to select out deuterons and typical scatter plots are shown in figure 1. The small cluster of events with smaller pulse heights and shorter times of flight correspond to protons. About 95% of the events passed the PID test. THTPHI is a box cut on the horizontal and vertical scattering angles at the target and a scatter plot is shown in figure 2. The events and the box in the THTPHI plot are not centered about the

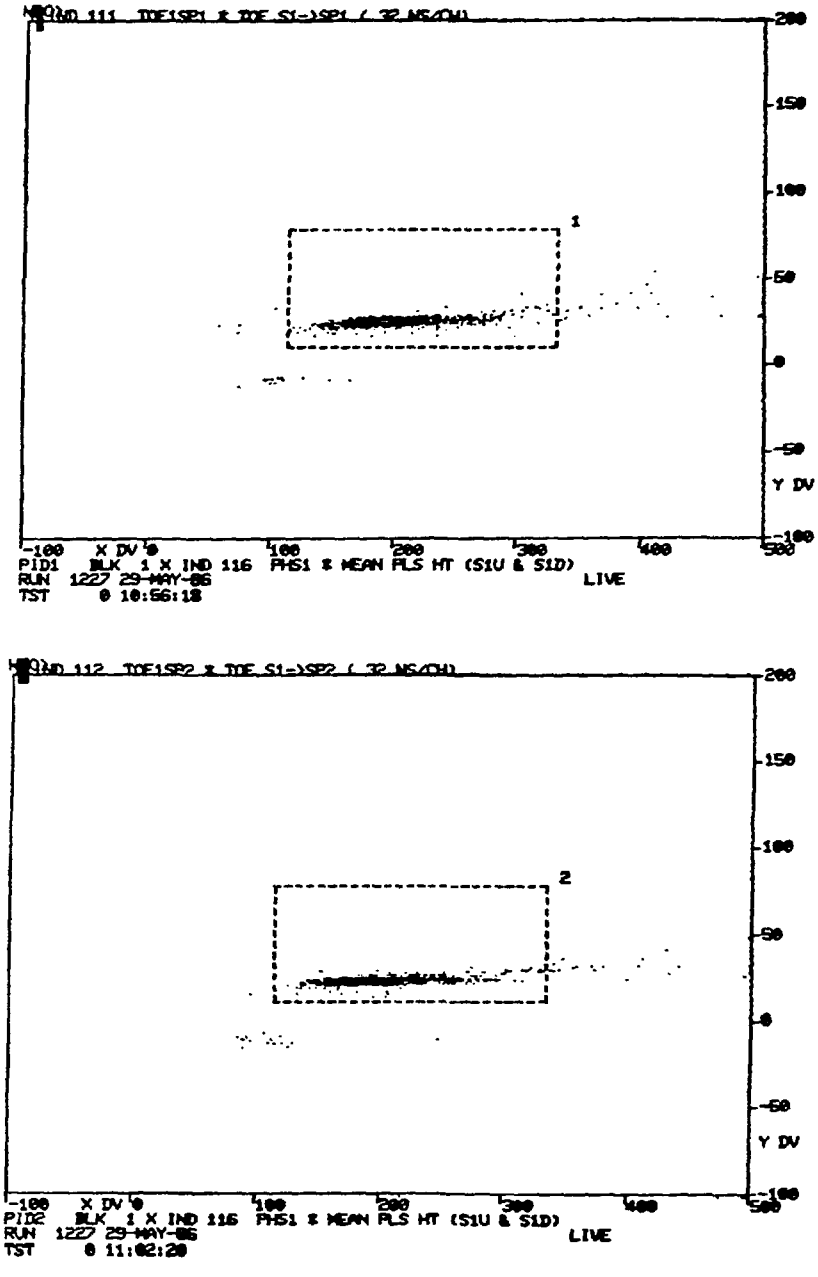

Figure D-1

PID boxes. The vertical axis is the time of flight from S1 to SP1 (top) or SP2 (bottom) and the horizontal axis is the pulse height in S1.

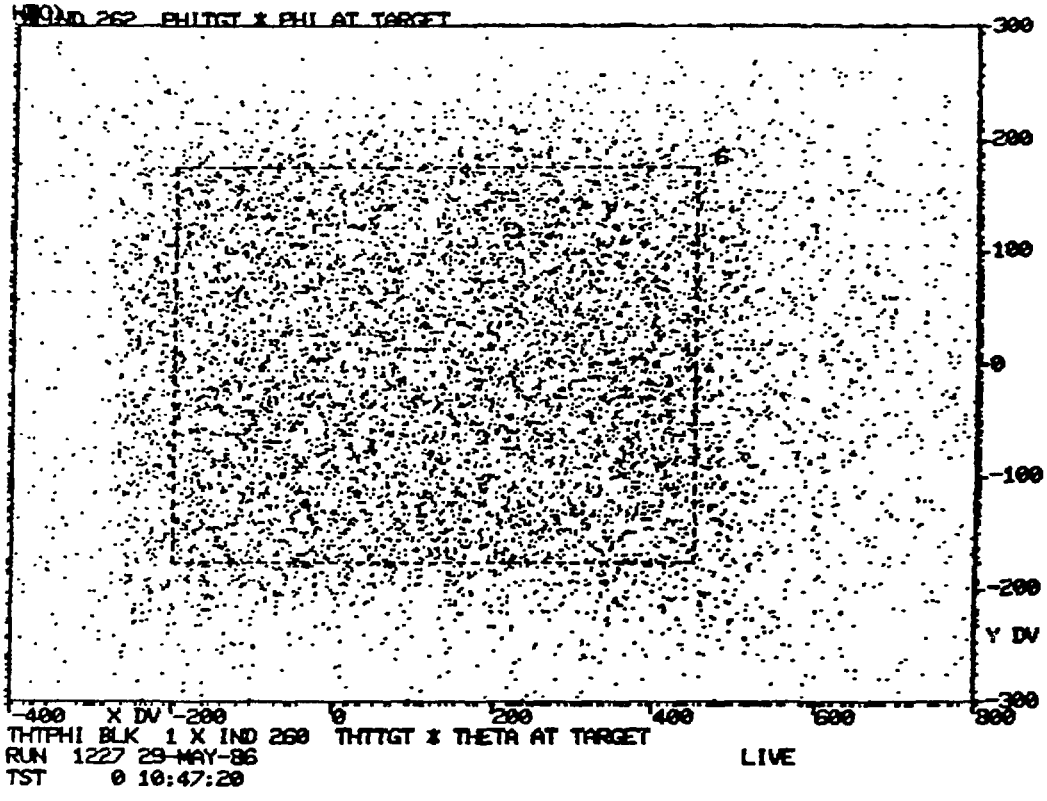

Figure D-2

THTPHI box. The horizontal and vertical axis are the vertical and horizontal scattering angles at the target. Units are 0.1 mrad.

origin because the calculations of the vertical and horizontal scattering angles contain the offsets discussed in chapter VI. However, the distribution of events and the sizes of the offsets indicate that the box is centered well within 0.2 degrees of the true center of the spectrometer acceptance.

Asymmetries were obtained by fitting the missing mass spectra using the code ALLFIT as described in chapter VII. The spectrum was assumed to consist of a background and a proton-deuteron elastic peak which was parameterized in the same way as those at the other angles. The peak shape and position were allowed to vary but were required to be the same on the normal and reverse spectra while the peak heights were allowed to vary independently. The background shape was obtained by fitting runs taken with the mock target filled with non-deuterated propanediol. The same background shape was used for normal and reverse spectra and for all runs. A typical spectrum and fit are shown in figure 3.

Most of the runs were fit using the yield normalization discussed at the beginning of chapter VII both to establish the normal to reverse background level ratio and to calculate the asymmetry. Only the average background level was allowed to vary in these fits. All spectra could not be fit in this way because the first few runs were taken without the ion chambers used to monitor the beam intensity. Asymmetries for these spectra were obtained by allowing the two background levels to vary independently during the fit. These levels were then used as the normalization for the calculation of the

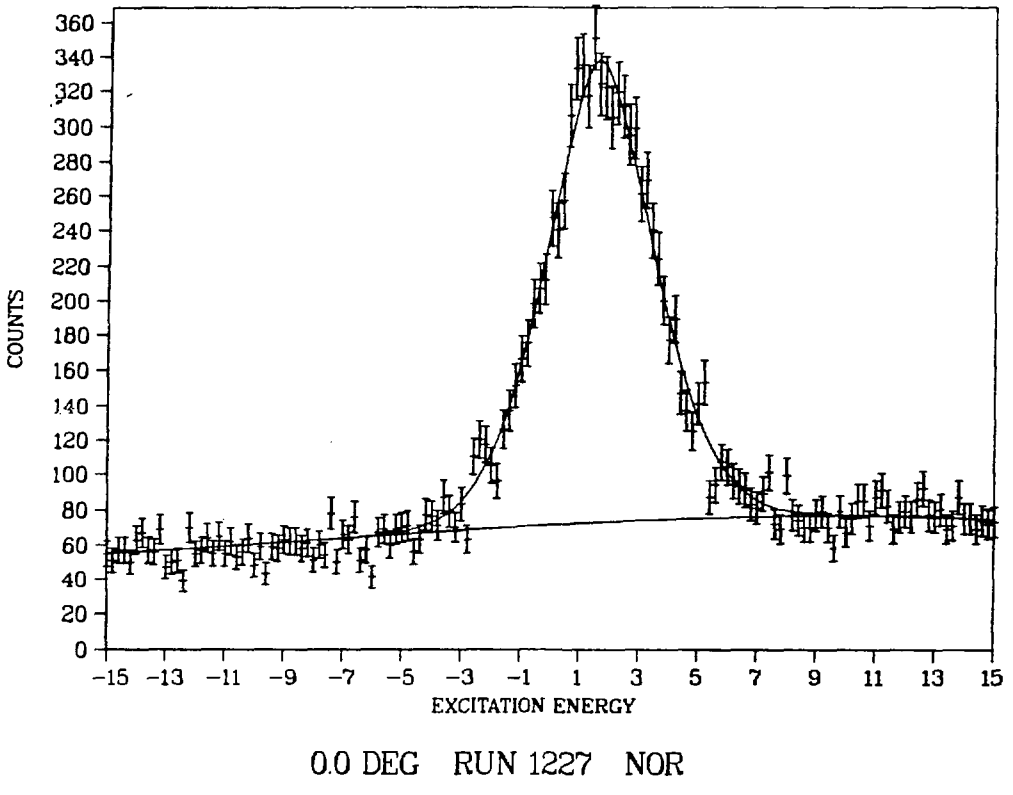

Figure D-3

Typical fit of a backward scattering spectrum. The units on the horizontal scale are MeV.

asymmetry. The spectra taken with the ion chambers in were also fit in the second manner as a check and the agreement between the two was quite good.

Calculation of A_{LL}

The general expression, II-1, giving the parity invariant cross section for scattering from an L-type target is simplified at 180 degrees:

$$Y = Y_0 \left[1 + \frac{3}{2}A_{LL}P_L P + \frac{1}{2}A_{0LL}P_T\right] .$$

If the acceptance is finite and not centered, then other terms which depend on the beam polarization may contribute. However, these contributions tend to be small because they must vanish at 180 degrees and must have opposite sign on opposite sides of this point. From this expression, we calculate the usual asymmetry due to the beam polarization:

$$\varepsilon = \frac{\frac{3}{2}A_{LL}P_L P}{1 + \frac{1}{2}A_{0LL}P_T} .$$

This expression can be made linear in the observables if we allow the right hand side to have a slight dependence on the asymmetry:

$$\varepsilon = \frac{3}{2}A_{LL}P_L P - \frac{1}{2}A_{0LL}P_T\varepsilon .$$

This equation was used as the basis for a least squares fit as described in appendix E. The uncertainties in the beam and target polarizations as well as those in the asymmetries were included.

The fit in which both analyzing powers were free to vary gave a value of -0.30 ± 0.04 for A_{LL} and -0.46 ± 3.19 for A_{0LL}. Because the uncertainty for A_{0LL} is very large, fits were also made with this parameter fixed. Such fits are equivalent to taking weighted averages because only one free parameter remains. The value of A_{0LL} was taken to be -1.0, 0.0, and 1.0 and the resulting values for A_{LL} were -0.289, -0.301, and -0.313, respectively, each with an uncertainty of 0.012. Using these values and including in quadrature the systematic uncertainties described in appendix B, we obtain the more precise result,

$$A_{LL} + 0.012\ A_{0LL} = -0.301 \pm 0.015\ .$$

If the acceptance is not symmetric in either the vertical or horizontal scattering angle, then the measured asymmetry may include contributions from other analyzing powers. As a check, a least squares fit was also done based on equation 2 of chapter IX with A_{0LL} and A_{NLL} fixed at zero. The value for A_{LL} changed by less than the uncertainty in the above expression and all other analyzing powers were found to be zero within their uncertainties.

E. Least Squares Fit

The asymmetries and outgoing polarizations which we measure both have a linear dependence on the observables of interest. The coefficients multiplying the observables depend on the beam and target polarizations, the deflection and spin precession of the protons in the magnetic fields, and the yield ratios. Here we detail the linear least squares fit used to extract the observables from our measurements.

The measurement y has a linear dependence on the observables C_α which we wish to determine:

$$y = \Sigma\, x_\alpha C_\alpha \ .$$

The method of least squares finds the values of the observables which minimize the chi square defined by

$$\chi^2 = \Sigma\, w_i\, (y_i - \Sigma\, x_{\alpha i} C_\alpha)^2 \ . \qquad (1)$$

The sum is taken over all measurements labelled by the index i. The reduced chi square is obtained by dividing the chi square by the number of degrees of freedom which is defined as the number of measurements minus the number of free parameters.

We solve this minimization problem in the usual way. Requiring the derivative of chi square with respect to each C_α to be zero gives

$$v_\beta = \Sigma\, M_{\beta\alpha} C_\alpha \qquad (2)$$

where $v_\beta = \Sigma\, w_i y_i x_{\beta i}$ and $M_{\beta\alpha} = \Sigma\, w_i x_{\beta i} x_{\alpha i}$. The C_α are then obtained from equation 2 by inverting the matrix M. The inverse of M is the error matrix.

If we neglect uncertainties in the coefficients $x_{\alpha i}$ and assume the uncertainty in the measurement y_i has a gaussian distribution, then equation 1 follows from maximum likelihood. With these assumptions, the weight factor w_i is the reciprocal of the square of the standard deviation of the measurement y_i. The diagonal elements of the error matrix then give the squares of the standard deviation uncertainties in the observables and the off diagonal elements give the error correlations:

$$\langle (C_\alpha - C_\alpha^*)(C_\beta - C_\beta^*) \rangle = (M^{-1})_{\alpha\beta} \, .$$

Here C_α^* is the true value of C_α.

However, for our measurements, uncertainties in the coefficients $x_{\alpha i}$ can make the uncertainty in the right hand side of equation 1 comparable to that of the left. To account for this, we replace the uncertainty in y_i with that in the difference $y_i - \Sigma\, x_{\alpha i} C_\alpha$. I.e., by assuming this difference has a gaussian distribution and invoking maximum likelihood, we are led to define the weight factor w_i as the inverse square of the standard deviation uncertainty in the difference. This uncertainty includes contributions from

uncertainties in the beam and target polarizations and the yield ratio as well as that in the asymmetry or outgoing polarization.

The only drawback of this technique is that the weight factors now depend on the values of the observables C_α. We neglect this dependence when taking the the derivatives to minimize chi square and again obtain equation 2. If the final values of the observables differ significantly from those used to calculate the weight factors, then the new values are used to recalculate these factors which are then used to recalculate the observables. This procedure converges quickly. The interpretation of the final error matrix M^{-1} is the same.

ACKNOWLEDGEMENTS

I would like to thank my advisors Chuck Whitten and George Igo for providing me the opportunity to work on this project and for their support throughout the effort. The guidance and assistance of the UCLA postdocs Bjarne Aas and Franz Sperisen are also very gratefully acknowledged. I thank all the LAMPF staff associated with this and other UCLA experiments especially Kevin Jones, John McClelland, Noby Tanaka, and Jim Amann. I also thank Marek and Elizabeth Bleszynski both for their theoretical calculations and their guidance of my efforts.

In addition to the above, I would like to thank all the other participants in the experiment discussed here. These include H. Fujisawa, M. Gazzaly, S. J. Greene, H. Hasai, A. Masaike, C. Newsom, Y. Ohashi, S. Okumi, and G. Pauletta.

I thank Bea Blonsky, Penny Lucky, Gloria Garcia, Maggie Eutsler, and all the other administrative staff at UCLA and LAMPF who have assisted me during my stays at those institutions. I would also like to thank all the staff at the LAMPF data analysis center for their help with this and other projects.